\$ SUPER

Contents lists available at ScienceDirect

Journal of Geochemical Exploration

journal homepage: www.elsevier.com/locate/gexplo



Trace element signatures in scheelite associated with various deposit types: A tool for mineral targeting

Ana Carolina R. Miranda ^{a,b,*}, Georges Beaudoin ^{a,b}, Bertrand Rottier ^{a,b}, Jan Pašava ^c, Petr Bohdálek ^c, Jan Malec ^c

- a Département de Géologie et Génie Géologique, Université Laval, Québec, Canada
- ^b Centre de recherche sur la géologie et l'ingénierie de ressources minérales (E4m), Université Laval, Québec, Canada
- ^c Czech Geological Survey, Geologická 6, CZ-15200 Praha 5, Czech Republic

ARTICLE INFO

Keywords: Scheelite Trace element indicator mineral PLS-DA Random forest

ABSTRACT

Scheelite is a widespread mineral in several geological settings and its trace element composition provides valuable information about the source and composition of the hydrothermal fluids. In this study, scheelite from 22 magmatic-hydrothermal deposits and 2 orogenic Au deposits (Hangar Flats and Corcoesto) were analyzed by EPMA and LA-ICP-MS. Magmatic-hydrothermal scheelite, together with literature data are investigated using partial least square-discriminant analysis (PLS-DA) and Random Forest (RF) classifier, to evaluate the use of scheelite as a robust indicator mineral for W-bearing deposit targeting. Cathodoluminescence images show that scheelite is texturally homogeneous in reduced intrusion-related gold systems (RIRGS) and varies from homogeneous to heterogeneous in other magmatic-hydrothermal and orogenic Au deposits. Scheelite displays six REE chondrite-normalized patterns, which are a function of the source and composition (mainly salinity) of the mineralizing fluids and partitioning with co-genetic minerals (e.g., garnet, clinopyroxene). The PLS-DA highlights that scheelite trace element composition from magmatic-hydrothermal deposits varies following different deposit types (e.g., oxidized and reduced skarns, porphyry W-Mo, RIRGS, quartz-vein/greisen Sn-W), and that such compositional variation reflects mainly the difference of fO2 and composition of mineralizing fluids. Additionally, scheelite from magmatic-hydrothermal deposits are chemically distinct to those formed dominantly by metamorphic fluids in orogenic settings as shown by their higher Mo, Nb and Mn, and lower Sr contents and predominantly negative Eu anomalies. Metamorphic scheelite can be discriminated from that of orogenic Au deposits by their lower Pb, As and REE contents and LREE/HREE ratios, which are related to local host rock composition and metamorphic grade. Using Na, Mg, Mn, As, Sr, Y, Nb, Mo, Pb, ΣREE concentrations and Eu anomaly as predictors, the RF model yields an overall prediction accuracy of 97 % for test data as function of deposit types (89.2 % for RIRGS, 100 % for porphyry W—Mo, 97.8 % for quartz-vein/greisen Sn—W, 96.9 % for oxidized skarn, 98.1 % for reduced skarn and 99.3 % for orogenic Au deposits). Application of RF classifier to scheelite composition from orogenic Au and skarn- and greisen-type W deposits from literature yields an overall prediction of \sim 79 % (91 % for oxidized skarn, 71.4 % for quartz-vein/greisen Sn—W and 74.2 % for orogenic Au deposits) showing that scheelite is an efficient indicator mineral for Au and W deposits targeting. Metamorphic scheelite is predicted mostly as orogenic Au scheelite (83 %), reflecting the genesis of metamorphic fluids and similar geological setting, suggesting that RF classifier can be also used to predict the fluid sources.

1. Introduction

Advances in micro analytical techniques have allowed a better chemical characterization of minerals and consequently, a better understanding of ore-forming processes (Gaspar et al., 2008; Dare et al., 2012; Andersson et al., 2019; Mansur et al., 2021). Such approach has

been applied in several fields of economic geology to assess the fertility of igneous rocks to form mineral deposits (e.g., zircon, Ballard et al., 2002 and Wade et al., 2022; epidote, Cooke et al., 2014), vector towards mineralized systems (Cooke et al., 2014; Wilkinson et al., 2015; Rottier and Casanova, 2020), discriminate and indicate distinct types of mineral deposits (Belousova et al., 2002; Dupuis and Beaudoin, 2011; Boutroy

^{*} Corresponding author at: Département de Géologie et Génie Géologique, Université Laval, Québec, Canada. E-mail address: acrmiranda1@gmail.com (A.C.R. Miranda).

et al., 2014; Dare et al., 2012, 2014; George et al., 2015, 2018; Pašava et al., 2016; Huang et al., 2019; Mansur et al., 2020; Barnes et al., 2022; Mansur et al., 2023) and to prospect/target mineral deposits in regional exploration surveys (Duran et al., 2019; De Bronac et al., 2021). Several studies have shown that multivariate statistical and machine learning methods, specially random forest (RF), combined with mineral chemistry are successful not only in classification and prediction of deposit types (O'Brien et al., 2015; Mao et al., 2016; Gregory et al., 2019; Makvandi et al., 2019; Porter et al., 2020; Sciuba et al., 2020, 2021; Liu et al., 2021; Zhao et al., 2021; Bédard et al., 2022; Caraballo et al., 2022; Ghosh and Upadhyay, 2022; Miranda et al., 2022; Nathwani et al., 2022; Sun et al., 2022) but also to predict the fertility for ore deposits (O'Brien et al., 2015).

Scheelite (CaWO₄) is commonly found in magmatic-hydrothermal deposits (Noble et al., 1984; Hart, 2007; Song et al., 2014; Poulin et al., 2018), and metamorphic-hydrothermal orogenic Au deposits (Groves et al., 1998; Craw et al., 2015; Sciuba et al., 2020). Besides of being one the main mineral of W, which is considered a critical metal with high demand and moderate supply by European Commission (2017), several studies have highlighted the scheelite potential as an indicator mineral to target W and Au deposits (Averill 2001, 2011; McClenaghan et al., 2017; Maneglia et al., 2017; Grzela et al., 2019; Sciuba et al., 2020; De Bronac et al., 2021). Scheelite is a mineral resistant to mechanical abrasion and chemical weathering with a high density, and can be easily to be identified, making it a suitable indicator mineral that can survive long distance of transport and that be easily recovered from stream and glacial sediments. Additionally, because scheelite hosts several key trace elements (Mo, As, Nb, Sr, Na, Mn, Σ REE), it has been widely used to constrain the fluid source (Kent et al., 1995; Voicu et al., 2001; Scanlan et al. 2018; Elongo et al., 2022; Palmer et al., 2022), age (Bell et al., 1989; Darbyshire et al., 1996; Wintzer et al., 2022) and as a proxy for physic-chemical conditions in several geological settings (Brugger et al., 2008; Song et al., 2014; Kozlik et al., 2016a, b; Zhao et al. 2018; Miranda et al., 2022), in addition to discriminate different types of deposits (Kempe and Oberthur, 1997; Song et al., 2014; Poulin et al. 2018; Sciuba et al., 2020; Miranda et al., 2022; Nie et al., 2023).

The chemical composition of scheelite in orogenic Au and skarns deposits has been documented in detail (Ghaderi et al., 1999; Song et al., 2014; Poulin et al. 2018; Xu et al., 2019; Sciuba et al., 2020; Miranda et al., 2022). These contributions have shown the potential of scheelite chemistry as a useful exploration tool to discriminate, for instance, orogenic Au and skarn-related deposits. However, the chemical characterization of scheelite in several other ore deposit types such as RIRGS, quartz-vein/greisen Sn—W and porphyry W—Mo remains incomplete limiting its application as an efficient indicator mineral of the source of detrital scheelite.

This contribution aims to use the minor and trace elements composition of scheelite and assess its efficiency to predict deposit types using detrital scheelite in overburden sediments. Scheelite chemical composition from RIRGS, porphyry W—Mo, quartz-veins/greisen Sn—W and skarn-type deposits are combined with literature data to show that trace element in scheelite varies between different deposit types and settings. These data are investigated by partial least squares-discriminant analysis (PLS-DA) and RF classifier to discriminate mineral deposit types and other geological settings. The PLS-DA and RF classifier models are tested with scheelite chemistry data from two orogenic Au deposits (Hangar Flats and Corcoesto) and other deposit data from literature to assess their effectiveness. The results show that compositional variations of scheelite chemistry can be used to discriminate different deposit types, enabling its application in mineral exploration.

2. Geological features of scheelite-bearing samples

Scheelite from polymetallic skarn, quartz-vein/greisen Sn—W, porphyry W—Mo, RIRGS, and orogenic Au deposits, which cover the main

scheelite-bearing ore deposits, were analyzed (Fig. 1 and Table 1). Scheelite skarn samples are classified as oxidized and reduced skarns based on mineral assemblage and scheelite composition following Miranda et al. (2022). Reduced skarns are characterized predominantly by clinopyroxene, amphibole (Fig. 2a-b) and sulfides with minor garnet, whereas oxidized skarns consist mainly of garnet, clinopyroxene, amphibole and oxides (Table 1). Reduced and oxidized skarn scheelite samples comprise mainly exoskarns surrounding intermediate to felsic intrusions (Table 1). Skarn host rocks vary from dolostone/limestone to metasedimentary rocks and gneiss (Table 1). Five of the localities contain major W, Fe and Cu skarns deposits (Obří důl, Traversella, Kanbauk, Invincible Mine and Nui Phao), whereas six other investigated localities represent small deposits/showings. Nui Phao is the only deposit where scheelite mineralization occurs in both skarn and quartzveins/greisen (Nguyen et al., 2020).

Machwi, Kirwans Hill, Zinnwald and Nui Phao contain typical greisen-type Sn—W mineralization associated with highly evolved F- or B-rich felsic intrusions (Table 1). Scheelite occurs disseminated and associated with micas, cassiterite, wolframite and fluorite in greisenized cupolas of the felsic intrusions. At Felbertal, scheelite mineralization occurs mainly in quartz-veins and disseminated throughout orthogneiss and amphibolite (Kozlik et al., 2016a, 2016b), and was formed at 335 Ma from W-rich fluids derived from orthogneiss (Raith et al., 2011). Late metamorphic events at 330 Ma and 30 Ma are recorded in scheelite, which caused its partial recrystallization (Raith et al., 2011; Kozlik et al., 2016a, 2016b). The analyzed Felbertal samples comprise primary scheelite and recrystallized crystals from the first metamorphic event (Fig. 2c).

The RIRGS samples are from the Tintina Gold belt, located between Yukon (Canada) and Alaska (USA), and from the Čelina deposit (Czech Republic; Fig. 1). Reduced IRGS comprise a variety of deposit styles, which range from intrusion-hosted sheeted quartz veins and skarn to proximal hornfels-hosted replacement/disseminated mineralization, and distal Au-As-Sb veins (Thompson et al., 1999; Hart et al., 2000, 2002; Lang and Baker, 2001). The scheelite-bearing samples cover the majority of these deposit styles with intrusion-hosted sheeted quartz-veins from Dublin Gulch and Fort Knox; scheelite-bearing clinopyrox-ene/amphibole skarn (Fig. 2d) and marble from Fort Knox, Scheelite Dome and Colbert Lode; and disseminated/quartz-vein style from Čelina and Gil-Sourdough (Alaska; Table 1).

The two porphyry W—Mo examples investigated are Northern Dancer and Jennings, located in Yukon, Canada (Table 1). Both deposits are derived from the same suite of quartz monzonite to monzogranite rocks emplaced in sedimentary rocks at 110–120 Ma (Noble et al., 1984; Mihalynuk and Heaman, 2002). The tungsten mineralization occurs as a system of quartz-scheelite veins with variable amounts of plagioclase, pyrite, and beryl, which is hosted in both intrusion and nearby hornfels (Noble et al., 1984).

Corcoesto (NW Spain) is an orogenic Au deposits where Au mineralization is related to extensional zones, which represent second order dextral shear bands. Scheelite crystals (Fig. 2e) occur in quartzarsenopyrite veins within leucocratic orthogneiss that pre-date Au mineralization (Boiron et al., 1996, 2003; Cepedal et al., 2014). Hangar Flats (Idaho, USA) is also an orogenic Au deposit (Wintzer et al., 2022) that hosts significant Sb, Ag and W resources (Table 2). The Au-Sb-W mineralization is controlled by faults and hosted in brecciated granodiorite (Wintzer et al., 2022). The W mineralization (57 Ma) post-dates the Au mineralization (67–58 Ma), and both are crosscut by late W—Sb veins suggesting distinct mineralized events (45 Ma; Gillerman et al., 2019; Wintzer et al., 2022). The analyzed scheelite-bearing samples are from the early W mineralization event. Stibnite occurs mostly in the matrix of brecciated scheelite of the first W mineralization (57 Ma), indicating that this stibnite was deposited after scheelite (Wintzer et al., 2022; Fig. 2f). In the late W-Sb veins (45 Ma), scheelite is intergrown with stibnite (Wintzer et al., 2022).

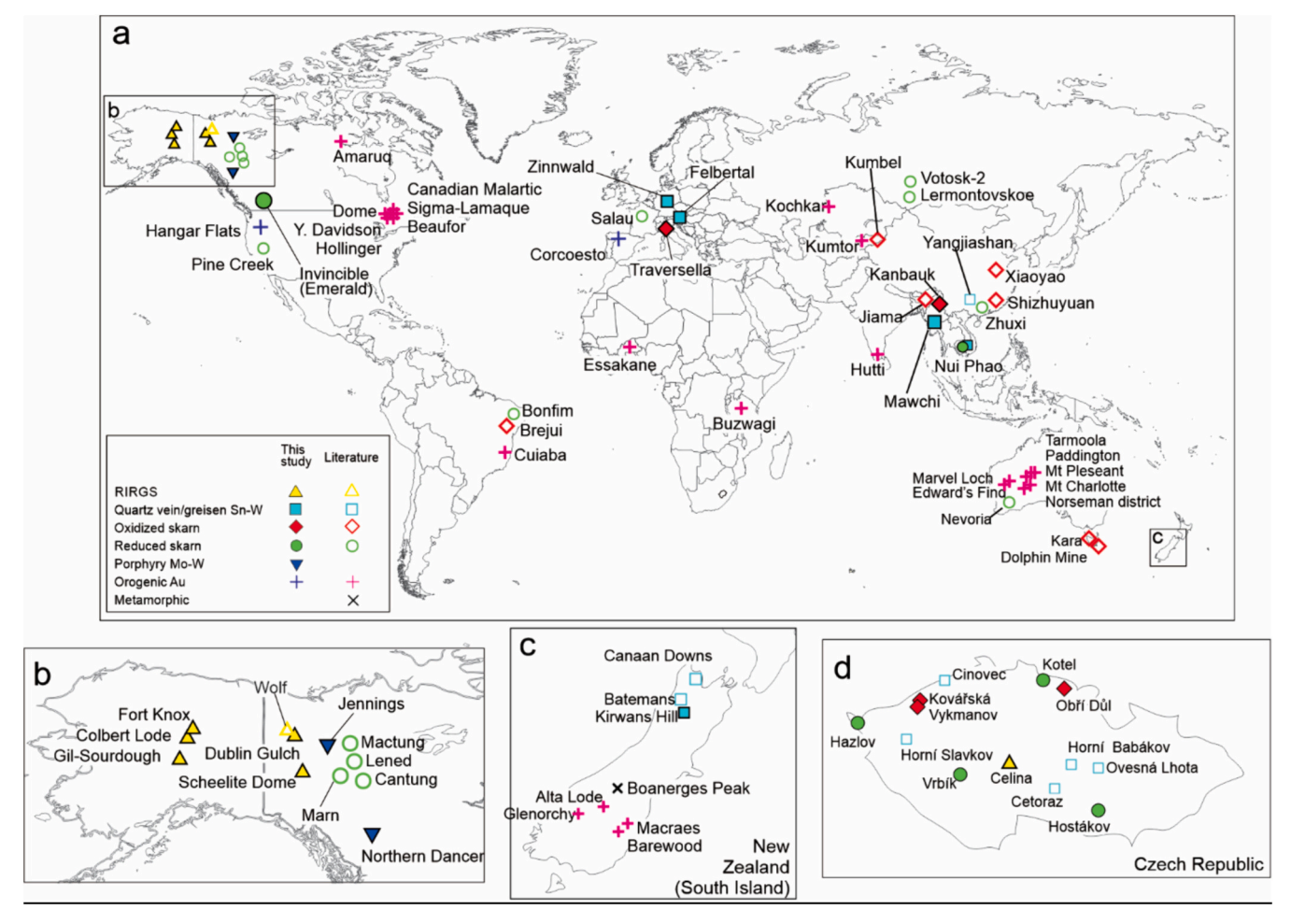


Fig. 1. a. World distribution of scheelite-bearing ore deposits samples considered in this study. Filled symbols represent scheelite-bearing ore deposit analyzed in this study, whereas empty symbols refer to scheelite-bearing ore deposits compiled from literature (ESM Table A4). b- d. Samples location from Alaska-Yukon (b), New Zealand (c), and Czech Republic (d).

3. Methodology

3.1. Samples

Sixty scheelite-bearing samples from 16 well-documented mineral deposits and 6 showings distributed worldwide were investigated (Fig. 1). The selected samples cover distinct deposit types, which include eleven skarns, five quartz veins/greisen Sn—W, four RIRGS districts and two porphyry W—Mo (see Table 1). Moreover, we also analyzed scheelite from two orogenic Au deposits: Corcoesto (2 samples) and Hangar Flats (2 samples; Fig. 1; Table 1).

3.2. Analytical Methods

Cathodoluminescence (CL) images and major (CaO and WO₃) and minor (Na, Sr, Mo and Fe) elements composition (n=140 analysis) of scheelite were determined using a CAMECA SX-100 electron probe micro-analyser (EPMA), equipped with five wavelength-dispersive spectrometers (WDS) and a CL detector, at Université Laval, Canada. The analytical conditions for CL images were using an accelerating voltage set at 15 kV and the beam current at 20 nA with a working distance of 2 mm. The major elements were determined using a 10- μ m-diameter beam, 20 nA for beam current and 15 kV for accelerating voltage. The counting times were of 20 s at the peak and 10 s at the background. The analytical conditions for minor elements were using a 10- μ m-diameter beam, 100 nA beam current, 15 kV of accelerating

voltage, and counting times of 120 s at the peak and 30 s at the background. Metal tungsten (W), diopside (Ca), metal molybdenum (Mo), celestite (Sr), albite (Na) and magnetite (Fe) were employed as standards.

The minor and trace elements concentrations in scheelite (n = 432analyses) were determined by LA-ICP-MS using an Excimer 193 nm RESOlution M-50 laser ablation system equipped with a double volume cell S-155 and coupled with an Agilent 7900 mass spectrometer at the LabMaTer, Université du Québec à Chicoutimi (UQAC). The LA-ICP-MS tuning parameters were a laser frequency of 15 Hz, a fluence of 3 J/cm², and scanning speed of 10 μ m/s for the line scans. Depending on scheelite grain size, spots and line scans were made with beam sizes of 33 and 55 μm. Given the heterogeneous textures in scheelite revealed by CL images, the spots were performed in all distinct CL zones to obtain most variance as possible in scheelite composition. Iolite v3 running in Igor Pro 6.37 was used for data reduction (Paton et al., 2011). The following 118, 23Na, 24Mg, 39K, 44Ca, 49Ti, 51V, 55Mn, 57Fe, 59Co, 61Ni, 63Cu, 66Zn, 75As, 85Rb, 88Sr, 89Y, 93Nb, 95Mo, 137Ba, 139La, 140Ce, 141Pr, 146Nd, 147Sm, 153Eu, 157Gd, 159Tb, 163Dy, 165Ho, 166Er, 169Tm, 172Yb, 175Lu, 181Ta, 182W, 183W, 208Pb, 209Bi, 232Th and $^{\rm 238}\text{U}.$ The $^{\rm 44}\text{Ca}$ was used for internal standardisation for scheelite based on EPMA results (ESM Table A1), whereas Si and S were monitored to identify possible silicate and sulfide inclusions, respectively. The NIST-610 synthetic glass reference material was employed as external standard for all elements using preferred values from the GeoReM database (Jochum et al., 2005). The basalt glasses GSE-1 g, GSD-1 g and Gprobe6-

Table 1
Summary of the main geological characteristics of scheelite-bearing samples.

Deposit/ country	Major metal	Mineral association	Intrusion	Host rock	Age	Number of analysis	Deposit size	Temperature and salinity of the fluids	Reference
Quartz-vein/Gre	eisen W-Sr	ı							
Mawchi (Myanmar)	Sn-W	wo + sch + moly+apy + py + fl + dn	Peraluminous biotite granite and tourmaline granite	Granite and metasedimentary rocks	42 Ma	15	-	260–345 °C; 4.5–15.7 wt% NaCl eq.	Myint et al. (2018)
Nui Phao (Vietnam)	W-Bi- Cu-F- (Au)	qz + sch + fl	Peraluminous granite	Shales, sandstones, siltstones, marbles, and siliceous rocks	85 Ma	10	87.9 Mt. at 0.19 % WO ₃ , 7.95 % CaF ₂ , 0.18 % Cu, 0.19 g/ t Au, and 0.09 % Bi	275–337°C; 4.7–11.7 wt% NaCl eq.	Nguyen et al. (2020)
Kirwans Hill (New Zealand)	W	$\begin{array}{l} qz + sch + \\ ms + fl + tz \\ + tm \end{array}$	Granite	Granite and metasediments	382–358 Ma	12	-	-	Pirajno and Bentley (1985
Felbertal (Austria)	W	qz + sch + fl	Orthogneisses	Orthogneisses and amphibolites	335 Ma	62	6.1 Mt. at 0.5 % WO₃	-	Kozlik et al. (2016a,b)
Zinnwald (Germany)	Sn-W- Li	sch + qz	Strongly fractionated and slightly peraluminous rare metal A-type granites	Cínovec-Zinnwald granite cupola and rhyolite	312 Ma	12	-	370–410 °C; 0.4–5.6 wt% NaCl eq.	Webster et al. (2004); Breiter et al. (2017a, b)
Oxidized skarn				- 1 ·					
Obří důl (Czech Republic)	Fe-Cu- As-W	grt + cpx + amph+sch	Krkonoše-Jizera granite	Dolomite	312 Ma	79	0.1 Mt. of ore with 0.43–0.47 % W; 0.85 Mt. of ore with 0.41–0.43 % Cu and 0.19–0.49 % Bi	-	Veselovský et al. (2018)
Traversella (Italy)	Cu-Fe- W	cpx + sch + mag	Diorite	Dolomic marbles	30 Ma	12		300–625 °C	Dubru et al. (1988); Auwera and Andre (1991)
Kanbauk (Myanmar)	Sn-W-F	grt + px + amph+fl + sch	Biotite granite	Metasedimentary rocks	61 Ma	11	122 Mt. at 0.14 % WO ₃ , 0.23 % Sn, 11.57 % CaF ₂	-	Zhang et al. (2022); Technical report Savitar 2018
Kovářská (Czech Republic)	F-Ba- Fe-W	$\begin{array}{l} cpx + grt + \\ fl + sch \end{array}$	Bohemian massif/ Saxothuringian unit	Metamorphic crystaline basement (gneiss)	Variscan	3	Showing	-	Štemprok and Mašková (1992)
Vykmanov (Czech Republic) Reduced skarn	Zn-Pb- W	$\begin{array}{l} cpx + fl + \\ sph + gl + \\ sch + grt \end{array}$	Bohemian massif/ Saxothuringian unit	Metamorphic crystaline basement (gneiss)	Variscan	7	Showing	-	Štemprok and Mašková (1992)
Invincible Mine/ Emerald (Canada)	W-Mo (Au- Pb-Zn)	$\begin{array}{l} {\rm grt} + {\rm cpx} + \\ {\rm sch} \end{array}$	Cretaceous granite	Limestone	-	12	-	-	Ball (1954)
Nui Phao (Vietnam)	W-Bi- Cu-F- (Au)	amph+py + fl + sch	Peraluminous granite	Shales, sandstones, siltstones, marbles, and siliceous rocks	85 Ma	9	87.9 Mt. at 0.19 % WO ₃ , 7.95 % CaF ₂ , 0.18 % Cu, 0.19 g/ t Au, and 0.09 % Bi	275–337 °C; 4.7–11.7 wt% NaCl eq.	Nguyen et al. (2020)
Kotel (Czech Republic)	Cu-Fe- Zn	grt + cpx + sch	Krkonoše-Jizera granite	Limestone	312 Ma	12	Showing	-	Žáček (2008)
Hostákov (Czech Republic)	W	$\begin{array}{l} cpx + fl + \\ grt + ph + \\ sch \end{array}$	Třebíče massif, Ilmenite series	Metamorphic crystaline basement (gneiss)	Variscan	12	Showing	-	Štemprok and Mašková (1992)
Hazlov (Czech Republic)	W	ves + cpx + pl + wo + sch	Smrčiny granite massiv/ Moldanubian unit	limestone	Variscan	11	Showing	-	Štemprok and Mašková (1992)
Vrbík (Czech Republic)	W	sch + bt + amph+cc + po	Variscan Belt/ Central Bohemian granite pluton/ Moldanubian unit	metamorphic crystaline basement (gneiss)	Variscan	12	Showing	_	This study
Reduced Intrusio	on Related	l Gold Systems (R	RIRGS)						
Dublin Gulch (Canada)	Au-W	qz + sch + tn	Monzonite	Monzonite and limestone	94 Ma	8	1.5 Moz Au	141–345 °C; <15 wt% NaCl eq.	Maloof et al. (2001)
Scheelite Dome (Canada)	Au-W	cpx + sch	Monzonite	Limestone	94 Ma	22	4.1 Moz Au	300–550 °C; <4 wt% NaCl eq.	Mair et al. (2006)
Celine- Mokrsko	Au	qz + sch	Tonalite- granodiorite	Amphibolite	320–360 Ma	8	0.35 Moz Au	-	Lang and Baker (2001)

(continued on next page)

Table 1 (continued)

Deposit/ country	Major metal	Mineral association	Intrusion	Host rock	Age	Number of analysis	Deposit size	Temperature and salinity of the fluids	Reference
(Czech Republic)									
Fort Knox- Colbert Lode (USA)	Au-W	$\begin{array}{l} qz + sch \ \pm \\ amph \pm cc \end{array}$	Granodiorite	Monzonite and limestone	92 Ma	41	3.3 Moz Au	-	Thompson et al. (1999); Sims (2018)
Gil- Sourdough (USA)	Au	qz + ms + sch + py + apy	Granodiorite	Metasedimentary rocks	92 Ma	23	0.53 Moz Au (Measured and Indicated, Resources)	-	Allegro (1987); Blum (1985); Sims (2018)
Porphyry Northern Dancer (Canada)	W-Mo	$\begin{array}{l} qz+py+\\ sch+brl \end{array}$	Monzonite	Monzonite and limestone	110 Ma	13	242 Mt. at 0.10 % WO ₃ and 0.047 % MoS ₂	-	Noble et al. (1984); Mihalynuk and Heaman (2002)
Jennings (Canada)	W-Mo	qz + py + sch	Monzonite	Limestone	100 Ma	7	Drillhole intersected 234.0 m of 0.092%MoS ₂ and 0.110 % WO ₃ .	-	Roper (2008)
Orogenic gold Corcoesto (Spain)	Au	qz + sch + apy	-	Orthogeniss, biotitic gneiss and schists.		9	0.1 Moz	170–390 °C; 0.5–2.2 wt%	Boiron et al. (2003);
								NaCl eq.	Cepedal et al. (2014)
Hangar Flats/ Yellow Pine (USA)	Au-Sb- W	st + sch + pl	-	Brecciated granodiorite	56–45 Ma	17	1.6 Moz Au, 3.4 Moz Ag; 111.7 Mlb Sb; tungsten past production: 0.48 t W	-	Wintzer et al. (2022)

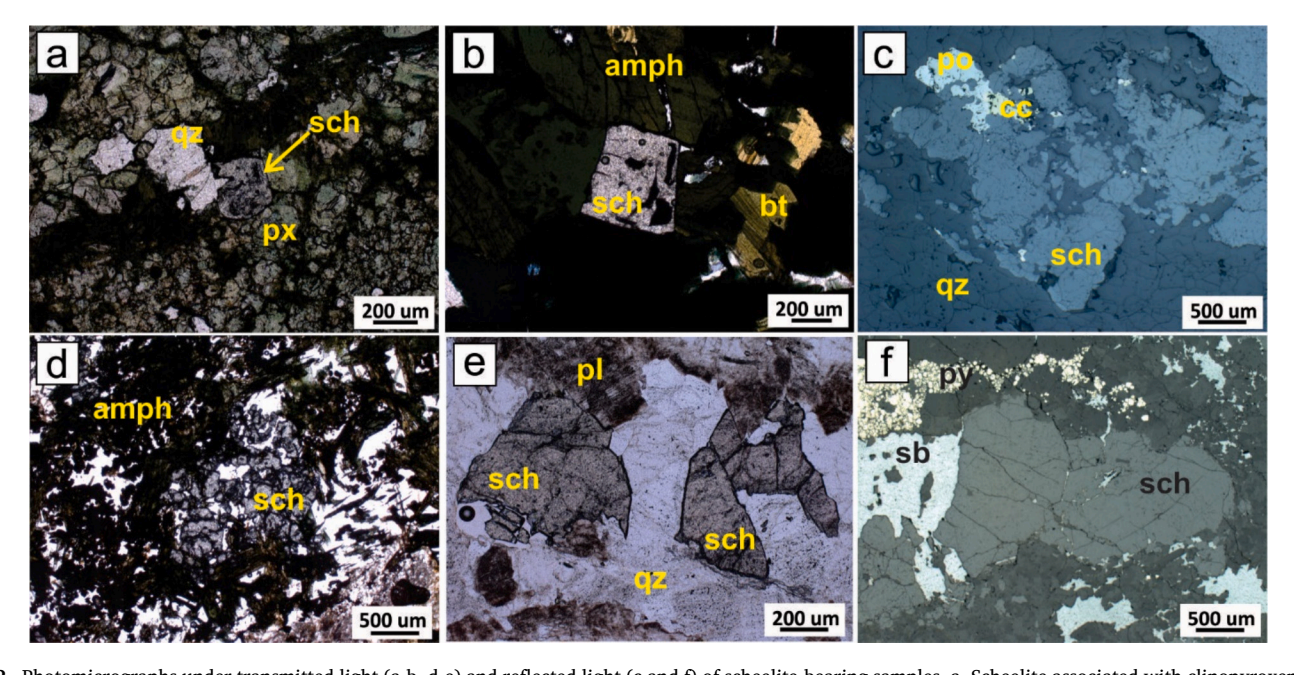


Fig. 2. Photomicrographs under transmitted light (a-b, d-e) and reflected light (c and f) of scheelite-bearing samples. a. Scheelite associated with clinopyroxene and few biotite from pyroxene skarn facies at Kanbauk. b. Scheelite crystal associated with amphibole and biotite from Nui Phao skarn. c. Coarsed scheelite grains associated with chalcopyrite, pyrrhotite and quartz from Felbertal quartz-vein W deposit. d. Scheelite associated predominantly with amphibole at Fort Knox. e. Scheelite crystals in a quartz-vein hosted in a granodiorite (Corcoesto). f. Scheelite with pyrite, stibnite and plagioclase from Hangar Flats. Abbreviations: sch: scheelite; grt: garnet; cpx: clinopyroxene; qz: quartz; mag: magnetite; amph: amphibole; po: pyrrhotite; cc: chalcopyrite; sb: stibnite; py: pyrite.

A and the NIST-612 (synthetic glass) were used as secondary reference materials for quality control. The reference materials were analyzed at the beginning, throughout and the end of each analytical session, to monitor a potential instrumental drift. The results obtained for the monitors were allowing for standard deviations on the working values. Detailed information about laser setting and reference material results

for quality control are presented in ESM Tables A2 and A3, respectively.

3.3. Statistical analysis

3.3.1. Data compilation and pre-processing Laser ablation-ICP-MS scheelite trace element composition data from

Deposit		Na (ppm)	Mg (ppm)	K (ppm)	Ti (ppm)	V (ppm)	Mn (ppm)	As (ppm)	Sr (ppm)	Y (ppm)	Nb (ppm)	Mo (ppm)	Ba (ppm)	Ta (ppm)	Pb (ppm)	Th (ppm)	U (ppm)	REE (ppm)
RIRGS	N	95	95	95	95	95	95	95	95	95	95	95	95	95	95	95	95	95
	Min	1.19	2.14	0.98	0.19	0.01	1.77	0.71	43.85	21.29	4.24	56.71	0.02	0.04	1.53	0.002	0.003	34.64
	Max	195.71	35.03	45.87	2.50	2.04	39.10	16.47	553.22	1120.34	212.25	5015.12	2.50	0.93	29.47	9.59	2.15	1469.6
	Median	24.74	4.34	10.01	0.75	0.16	11.19	2.63	151.51	92.16	21.98	1182.89	0.17	0.29	5.13	0.04	0.10	283.8
Porphyry W-Mo	N	20	20	20	20	20	20	20	20	20	20	20	20	20	20	20	20	20
	Min	64.50	79.79	1.91	1.06	0.23	12.57	3.42	57.69	341.38	165.41	277.58	0.01	0.54	2.27	0.11	0.06	1034
	Max	361.12	258.96	48.65	5.28	16.12	203.91	40.31	144.84	1223.2	1203.74	1473.40	6.89	12.95	30.57	625.50	18.90	3163
	Median	224.49	205.93	14.39	2.25	6.83	146.58	14.07	97.65	722.8	604.65	366.82	0.23	8.22	17.74	1.14	0.56	2200
Quartz vein/	N	111	111	111	111	111	111	111	111	111	111	111	111	111	111	111	111	111
Greisen Sn-W	Min	3.84	1.78	0.32	0.24	0.01	1.36	0.31	10.83	74.64	0.43	0.07	0.01	0.33	0.44	0.004	0.01	84.08
	Max	225.18	117.87	37.53	59.63	11.26	125.80	64.36	1380.27	2182.3	3210.90	15,721	6.67	86.18	87.15	151.51	262.71	3234.79
	Median	50.04	19.60	13.07	2.00	0.48	27.86	12.52	111.76	492.1	387.81	351.67	0.21	3.14	34.37	1.28	2.57	805.64
Oxidized skarn	N	112	112	112	112	112	112	112	112	112	112	112	112	112	112	112	112	112
	Min	0.55	0.02	0.26	0.33	0.01	0.27	0.07	13.96	0.03	1.37	21.82	0.01	0.36	0.67	0.004	0.001	3.24
	Max	305.80	129.27	83.40	18.07	6.12	224.90	362.79	159.16	1476	1167.60	53,932	48.65	35.31	236.30	8.28	16.68	2231.94
	Median	47.26	3.20	12.37	1.96	0.49	8.66	12.04	44.62	94.7	97.86	5281	0.12	0.83	4.92	0.15	0.07	409.46
Reduced skarn	N	68	68	68	68	68	68	68	68	68	68	68	68	68	68	68	68	68
	Min	0.44	0.02	0.37	0.20	0.001	0.26	0.27	33.92	0.39	1.43	3.22	0.01	0.34	0.64	0.002	0.001	0.82
	Max	84.79	244.64	41.70	12.51	1.39	52.50	7.37	1720.82	264.7	601.87	6296.7	3.61	4.96	127.88	11.13	15.82	965.80
	Median	9.40	3.54	9.80	1.20	0.05	10.19	1.44	77.01	17.94	25.82	325.82	0.18	0.48	2.36	0.05	0.09	163.84
Hangar Flats	N	17	17	17	17	17	17	17	17	17	17	17	17	17	17	17	17	17
	Min	7.88	6.03	2.66	0.32	0.001	0.26	0.16	1203.7	9.59	1.36	0.03	0.33	0.04	0.04	0.10	0.80	22.30
	Max	62.13	223.79	36.14	1.33	0.21	6.12	0.44	2855.1	61.16	1.77	0.85	1.97	0.25	0.57	1.71	11.76	100.57
	Median	31.14	22.94	13.76	0.58	0.00	0.35	0.24	2000	21.41	1.61	0.18	0.64	0.22	0.17	0.23	2.77	42.69
Corcoesto	N	9	9	9	9	9	9	9	9	9	9	9	9	9	9	9	9	9
	Min	15.10	26.69	2.92	0.70	0.04	12.52	4.23	32.93	134.55	17.79	9.24	0.01	0.45	4.24	0.04	0.01	488.10
	Max	64.91	80.76	51.43	4.59	0.14	17.39	14.18	40.18	950.76	37.67	45.87	0.14	0.52	5.70	0.72	2.36	1483.21
	Median	21.70	45.15	12.23	1.04	0.06	14.91	5.53	36.28	430.21	22.42	13.59	0.02	0.48	5.05	0.23	0.25	1049.23

this study and from Scanlan et al. (2018), Sciuba et al. (2020), Li et al. (2021), Palmer (2021), Miranda et al. (2022) and Pašava (unpublished data) were compiled and investigated with basic and multivariate statistics using Rstudio v4.04 (R Core Team, 2021). The literature data comprise 1620 trace element analyses of scheelite from eight quartz veins/greisen W—Sn, eighteen skarns, two RIRGS and twenty-eight orogenic Au deposits, and metamorphic scheelite (Fig. 1; ESM Table A4).

Log-ratio Expectation-Maximisation (lrEM) algorithm from R package zCompositions (Palarea-Albaladejo and Martin-Fernandez, 2013, 2015) was used to impute elements with <40 % below detection limit (bdl) values. Elements with over 40 % bdl values were excluded from further analysis. After imputation, the dataset was transformed using centred-log ratios (clr) to overcome the closure effect in compositional data (Aitchison 1986).

3.3.2. Partial Least-Squares Discriminant Analysis (PLS-DA)

The PLS-DA is a supervised multivariate dimensionality-reduction tool used for classification/clustering purpose. The method consists in finding the maximum variance of two matrices X (variables/elements) and Y (classes) that can be linked. Hence, the objective of PLS-DA method is to optimize the separation between the classes of samples and find the variables that best describe their differences. The results are visualized on scatter plots (loadings and scores plots) and bar plots (score contributions and variable importance on projection). The loadings plot illustrates the relationship between elements and groups, and the correlations among the elements. Hence, elements that plot in the same quadrant display a positive correlation, whereas those plotting on opposite quadrants display a negative correlation. The farther an element plots from the origin of the loading plot, the greater its contribution to the model, whereas the closer an element plot from the origin, the smaller its contribution for the classification. The scores plot displays the distribution of the samples in the space created by the variables and classes. Samples with similar features are grouped together (Eriksson et al., 2001). The score contribution plot highlights the differences between classes in relation to the average of the entire dataset. The Variable Importance on Projection (VIP) plot emphasizes the importance of each element for the model. Elements with VIP values >1 have major controls in separating the classes, whereas those between 0.8 and 1, and < 0.8 have intermediate and minor contributions in the discriminant analysis, respectively (Eriksson et al., 2001). The PLS-DA was conducted using the mixOmics package in R (Rohart et al., 2017).

3.3.3. Random Forest

Several studies have investigated the effectiveness of RF over other machine learning classifier algorithms such as Support Vector Machine, Artificial Neutral Network, Naïve Bayes, or Logistic Regression, in solving problems of classification and prediction applied to mineral deposits (Cracknell and Reading, 2014; Rodriguez-Galiano et al., 2015; Bédard et al., 2022; Nathwani et al., 2022). Therefore, er employed a RF classifier algorithm to test whether scheelite composition can be used for discrimination and prediction of deposit types.

Random Forest is a supervised machine learning algorithm that is commonly used for classification, regression, and prediction (Breiman, 2001). The algorithm consists of a large number of decision trees (forest) that operate as an ensemble. Each tree is individually built from a random sampling subset with replacement (bootstrapping) from the training dataset (i.e., analysis), and from randomly selected predictor variables (i.e., elements). The number (N) of predictor variables in each tree is set to be equal to the square root of the total variables of the training data (Breiman, 2001). The predictor variables and their values define each split (nodes) of the tree. Each decision tree searches through all candidates the optimal split that maximizes the purity of the resulting tree. Gini decrease is a measure that shows the contribution importance of each variable in the model. The higher the mean decrease Gini score, the higher importance of the variable in the model. The outcome of RF

model is visualized through a confusion matrix. The confusion matrix is built with the testing data, which is used to express the predictions of the classifier. The rows represent the true classes, whereas the columns indicate predicted classes.

Since RF performance does not require transformed data (Bédard et al., 2022), RF was performed using untransformed data and the Caret package in R (Kuhn, 2008). To build the RF model 70 % of the scheelite dataset was used as training data and 30 % was used for testing. The optimal configuration of model parameters was trained by a grid search procedure and validated by tenfold cross-validation technique. The best results for the RF model were acquired using 11 predictor variables (Na, Mg, Mn, As, Sr, Y, Nb, Mo, Pb, SREE and Eu anomaly) and 500 trees. In addition, scheelite from Corcoesto and Hangar Flats (this study), orogenic Au (Cave, 2016; Cave et al., 2017; Liu et al., 2021) and W greisen and oxidized skarn deposits (Huang et al., 2022), and metamorphic scheelite (Cave et al., 2017; Palmer, 2021) (ESM Table A5) were used as blind data to assess the effectiveness of the model. This additional dataset had few non analyzed elements (missing elements) that were imputed using missForest package in R, which is an algorithm specific to input missing elements (Stekhoven and Bühlmann, 2012). Similar to Random Forest algorithm, the missForest algorithm consists of building a random forest for each variable based on the input dataset and uses it to predict the missing variables.

4. Results

4.1. Cathodoluminescence and texture

In general, scheelite varies from fine to coarse grains regardless the deposit type (Fig. 2). Cathodoluminescence (CL) reveal textures varying from homogeneous to oscillatory zoning with less common recrystallization textures (Fig. 3). In quartz-vein/greisen Sn—W deposits, scheelite crystals are homogeneous or zoned (Fig. 3a), whereas at Felbertal, scheelite shows recrystallizations textures characterized by sub grains at the border of scheelite crystals (Fig. 3b). Under ultra-violet (UV) light, quartz-vein/greisen Sn—W deposits scheelite grains commonly display bluish colors. Scheelite from oxidized and reduced skarns are characteristically zoned, with common dissolution textures under CL (Fig. 3c-d). Under UV light skarn scheelite shows a yellow-greenish to bluish luminescence for oxidized skarns, and mostly bluish for reduced skarns.

Scheelite from RIRGS is predominantly homogenous under CL (Fig. 3e) and commonly display bluish color under UV light. At the Northern Dancer and Jennings porphyry W—Mo deposits, scheelite crystals vary from homogenous to zoned under CL (Fig. 3f) and displays mostly bluish luminescence color under UV light. At the Corcoesto orogenic Au deposit, CL reveals that scheelite crystals are commonly homogeneous (Fig. 3g). At Hangar Flats, scheelite occurs as aggregates of microcrystals and as coarse grains (Fig. 2f), and commonly displays oscillatory zoning under CL (Fig. 3h).

4.2. Composition variation in relation to deposit type

The full compositional data for scheelite is reported in ESM Table A5. The concentration ranges for each element grouped by deposit type are shown in box and whisker plots (Fig. 4) and Table 2. Also, the chemical variation of minor and trace elements of Hangar Flats and Corcoesto gold deposits are reported apart. In general, Mo is the most abundant minor element in scheelite from magmatic-hydrothermal deposits with concentrations ranging from 0.07 ppm to 5.4 wt%, followed by Nb (0.43 to 3211 ppm), Y (0.03 to 2182 ppm), Sr (10 to 1721 ppm), Th (0.002 to 625 ppm), As (0.054 to 363 ppm), Na (0.4 to 361 ppm), U (<0.001 to 263 ppm), Mg (0.02 to 259 ppm), Pb (0.03 to 236 ppm), Mn (0.25 to 225 ppm), Ta (0.03 to 86 ppm), K (0.28 to 83 ppm), Ti (0.14 to 60 ppm) and V (0.001 to 16 ppm).

The highest Mo content (from 21 ppm to 5.4 wt%) is associated with scheelite from oxidized skarns. Quartz vein/greisen Sn—W scheelite

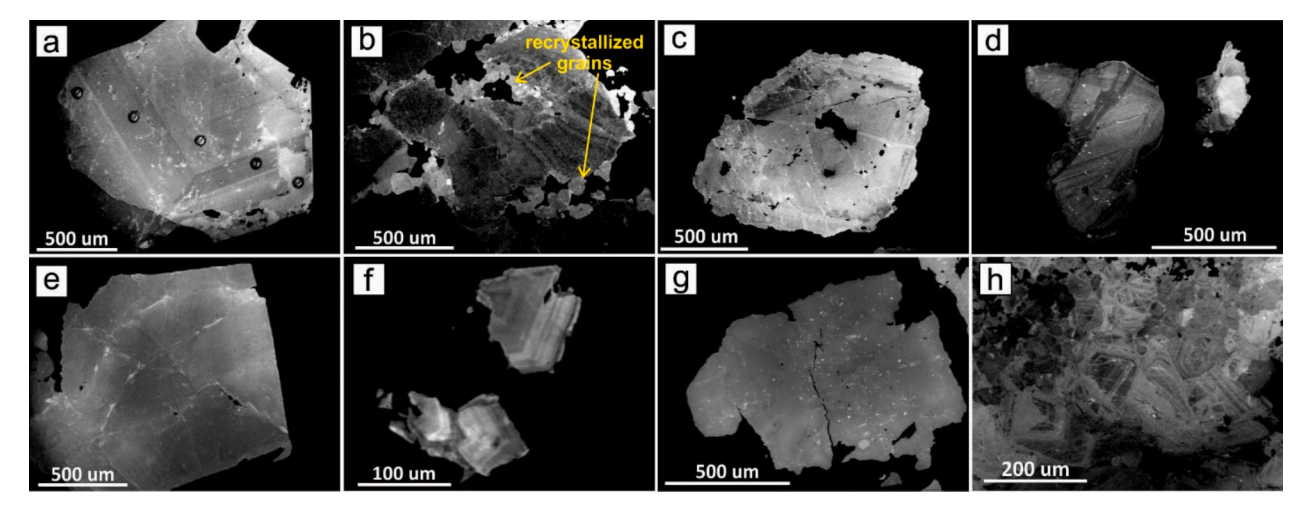


Fig. 3. Cathodoluminescence images of scheelite crystals. a. Scheelite with oscillatory zoning from Mawchi quartz-vein/greisen Sn—W. Laser spots on the grain. b. Zoned scheelite grain from Felbertal. Note recrystallized grains on the border with a light grey CL color. c. and d. scheelite with oscillatory zoning from Obří důl and Kotel (Krkonoše), respectively. e. Homogeneous scheelite crystal from Dublin Gulch (RIRGS). f. Oscillatory zoning in scheelite from Northern Dancer (W—Mo porphyry). g. Homogeneous scheelite crystal from Corcoesto orogenic gold deposit. h. Aggregate of zoned scheelite grains from Hangar Flats. (For interpretation of the references to color in this figure legend, the reader is referred to the web version of this article.)

displays the second highest Mo concentration which is up to 1.5 wt%, followed by reduced skarns (<6300 ppm), RIRGS (<5015 ppm) and porphyry W—Mo (<1500 ppm). The highest Nb content is associated with scheelite from quartz vein/greisen Sn—W (<3211 ppm), followed by porphyry W—Mo (<1204 ppm), oxidized and reduced skarns (<1168 ppm and < 602 ppm, respectively), and RIRGS (<212 ppm). Yttrium content is higher in quartz-vein/greisen Sn—W (74 to 2182 ppm) relative to oxidized skarn (0.03 to 1476 ppm), porphyry W—Mo (341 to 1223 ppm), and RIRGS (21 to 1120 ppm). Reduced skarn scheelite displays the lowest Y concentrations, ranging from 0.38 to 264 ppm.

Scheelite from reduced skarns and quartz vein/greisen Sn—W contain higher Sr content (1720 ppm and 1380 ppm, respectively) relative to scheelite from RIRGS (553 ppm), oxidized skarns (159 ppm) and porphyry (144 ppm). Thorium content varies from 0.1 to 625 ppm in porphyry W—Mo and from 0.003 to 151 ppm quartz-vein/greisen Sn—W scheelite. Scheelite from oxidized and reduced skarns and RIRGS display similar range of Th content, which varies between 0.002 and 11 ppm, with medians of 0.13 ppm, 0.05 ppm, and 0.04 ppm, respectively (Fig. 4). Arsenic concentration is higher in oxidized skarn (<362 ppm), quartz-vein/greisen Sn—W (<64.3 ppm) and porphyry W—Mo (<40.3 ppm) scheelite relative to RIRGS (<16 ppm) and reduced skarns (<8 ppm) scheelite, which display the lowest As contents.

The highest Na contents occur in scheelite associated with porphyry W—Mo (<361 ppm), followed by oxidized skarns (<305 ppm) and quartz-vein/greisen Sn—W (<225 ppm). Reduced-IRGS and reduced skarns scheelite display the lowest Na concentration, <195 ppm and <85 ppm, respectively. The highest U content occur in quartz-vein/greisen Sn—W (<263 ppm). Porphyry W—Mo and reduced skarns scheelite contain <19 ppm and < 16 ppm, respectively, and oxidized skarns and RIRGS scheelite display the lowest U concentration, <8 ppm and < 2.15 ppm, respectively. The highest Mg concentration occurs in scheelite from porphyry W—Mo (<258 ppm), followed by reduced skarns (<244 ppm) and oxidized skarns (<130 ppm). Quartz-vein/greisen Sn—W and RIRGS scheelite have the lowest content, up to 117 ppm and 35 ppm of Mg, respectively.

The highest Pb contents occur in scheelite from oxidized (<236 ppm) and reduced skarns (<128 ppm), followed by quartz-vein/greisen Sn—W (<87 ppm), porphyry W—Mo (<30.5 ppm), and RIRGS (<29.5 ppm). Manganese contents are higher in oxidized skarns (0.27 to 224 ppm), porphyry W—Mo (12 to 203 ppm), quartz-vein/greisen Sn—W (1.36 to 125 ppm) and reduced skarn scheelite (0.27 to 52.5

ppm) compared to scheelite from RIRGS (1.7 to 40 ppm). The Ta content is higher in quartz-vein/greisen Sn—W scheelite (<86 ppm for) relative to oxidized skarn (<35 ppm), porphyry W—Mo (<13 ppm), reduced skarn (<5 ppm) and RIRGS (<1 ppm) scheelite. The K contents are higher in oxidized skarn scheelite (<82 ppm), compared to porphyry W—Mo (<49 ppm), RIRGS (<46 ppm), reduced skarn (<42 ppm) and quartz-vein/greisen Sn—W (<38 ppm).

Titanium content varies from 0.23 to 60 ppm in quartz-vein/greisen Sn—W scheelite, from 0.33 to 18 ppm in oxidized skarn, and from 0.12 to 12.5 ppm in reduced skarn. The lowest Ti concentration occurs in scheelite from porphyry W—Mo (<5.3 ppm) and RIRGS (<2 ppm). Vanadium is less abundant element with concentrations not exceeding <16 ppm for porphyry W—Mo, <11.3 ppm for quartz-vein/greisen Sn—W, <6.1 ppm for oxidized and < 2 ppm for both reduced skarns and RIRGS scheelite.

The Σ REE contents in scheelite are variable, ranging from 0.81 to 3235 ppm. The highest concentrations occur in scheelite from quartz-vein/greisen Sn—W (84 to 3234 ppm), followed by porphyry Mo—W (1033 to 3163 ppm), oxidized skarn (3 to 2231 ppm) and RIRGS (34 to 1470 ppm). The lowest Σ REE content occurs in reduced skarn scheelite, with concentrations ranging from 0.81 to 966 ppm (Fig. 4).

A significant positive correlation occurs between Na and Σ REE-Eu + Y in scheelite from most oxidized skarn deposits, and few scheelite from RIRGS (Fig. 5a). No correlations are observed for RIRGS and oxidized and reduced skarns scheelite with low Σ REE-Eu + Y and Na contents (<30 ppm for Σ REE-Eu + Y, and < 10 ppm for Na). A positive correlation between Nb—Ta and Σ REE-Eu + Y is visible for most quartz-vein/greisen Sn—W, reduced and oxidized skarns and porphyry W—Mo scheelite (Fig. 5b).

Few chemical differences exist between Hangar Flats and Corcoesto scheelite. Molybdenum, Nb, Y, As, Pb, Mn, Ti and Σ REE contents are relatively higher in Corcoesto (<45.8 ppm of Mo, <37.6 ppm of Nb, <950 ppm of Y, <14 ppm of As, <0.7 ppm of Pb, <17.4 ppm of Mn, <5 ppm of Ti, and < 1483 ppm of Σ REE) compared to Hangar Flats scheelite (<0.85 ppm of Mo, <1.7 ppm of Nb, <61 ppm of Y, <0.44 ppm of As, <0.57 ppm of Pb, <6.1 ppm of Mn, <1.3 ppm of Ti, and < 100 ppm of Σ REE; Fig. 4 and Table 2), whereas Sr and U contents are higher in Hangar Flats (1200 to 2855 ppm of Sr, and 0.8 to 11.7 ppm of U) relative to Corcoesto scheelite (32 to 40 ppm of Sr and 0.01 to 2.3 ppm of U). Hangar Flats and Corcoesto scheelite contain similar concentration ranges of Th (from 0.04 to 1.7 ppm), Na (from 7.8 to 65 ppm) and K (2.6 to 51.4 ppm; Fig. 4).

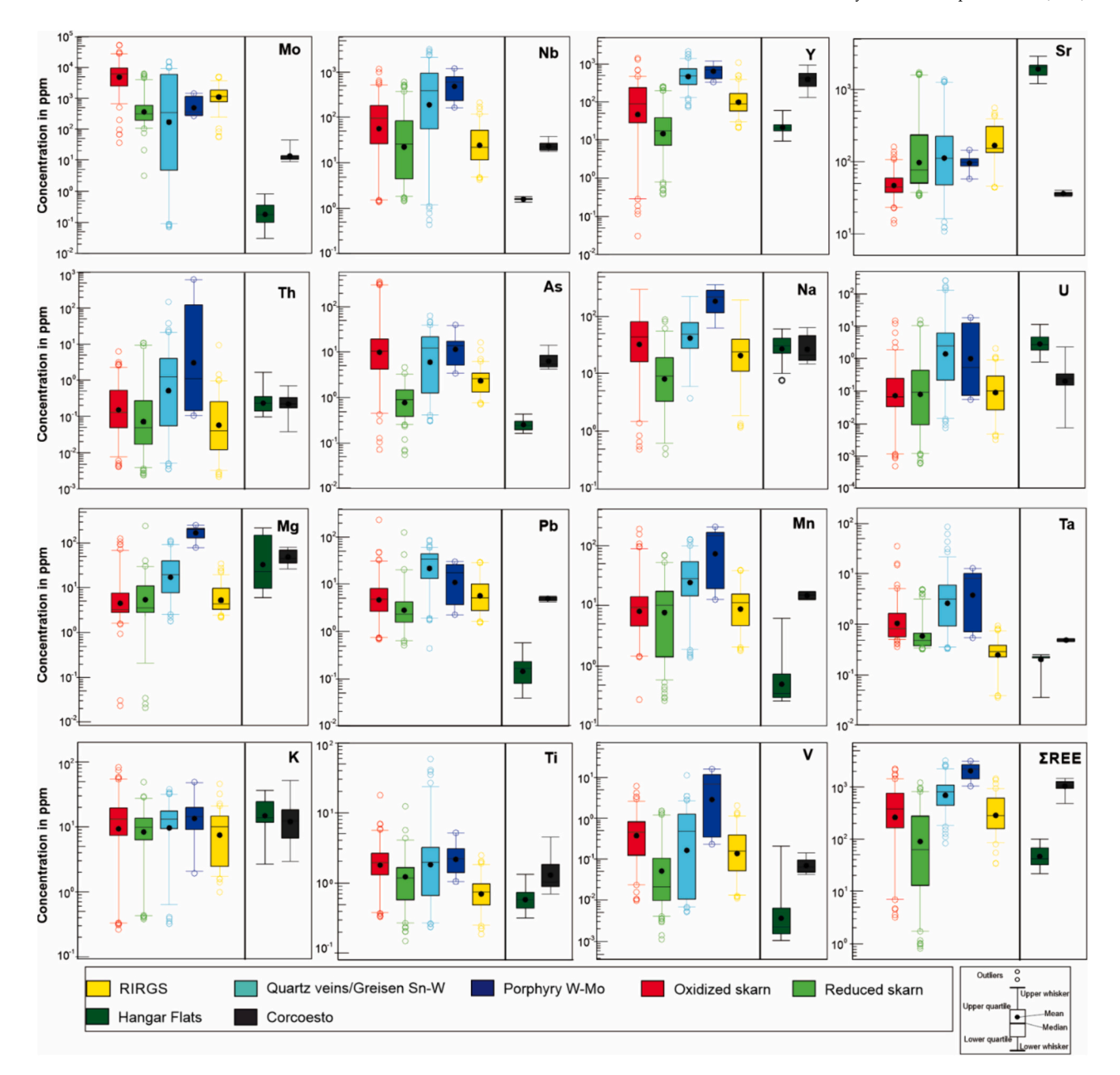


Fig. 4. Box and whisker diagram of trace elements concentrations in scheelite from magmatic-hydrothermal deposits and from Hangar Flats and Corcoesto.

Fig. 6 shows the relationship between few trace elements in scheelite that are useful to discriminate scheelite from different deposits. Scheelite data are from this study, including Corcoesto and Hangar Flats, in comparison to literature data (ESM Table A4). Overall, Mn and Nb are positively correlated for most magmatic-hydrothermal scheelite, whereas orogenic Au and metamorphic scheelite show no correlation (Fig. 6a). Niobium and Sr display a negative correlation for scheelite from magmatic-hydrothermal deposits (Fig. 6b). Similarly, Mn and Sr show a slightly negative correlation among magmatic-hydrothermal scheelite (Fig. 6c). Niobium and Mo contents increase from orogenic towards magmatic-hydrothermal scheelite (Fig. 6d), whereas the Sr content decreases from orogenic towards magmatic-hydrothermal scheelite (Fig. 6e). Hangar Flats scheelite plots in all diagrams with orogenic Au scheelite. In contrast, scheelite from Corcoesto plots more closely with magmatic-hydrothermal scheelite (Fig. 6a-e).

4.3. REE patterns

Scheelite from magmatic-hydrothermal deposits displays 6 REE patterns: (i) steep and (ii) shallow negative slopes, (iii) flat to slightly concave, (iv) concave, (v) convex, and (vi) positive slope (Fig. 7). The ESM Fig. A1 shows the REE patterns for individual deposit, and when available, the REE patterns for intrusions associated with mineralization. The steep negative slope pattern is characterized by La/Sm and Gd/Lu ratios >7, high La/Lu ratio (>300), negative Eu anomaly and is commonly displayed by scheelite from oxidized skarn deposits (Fig. 7a). The shallow negative slope pattern is characterized by La/Sm >0.7, given that some scheelite is slightly depleted in La relative to Sm, Gd/Lu >1, and La/Lu >2 ratios, positive and negative Eu anomalies, and is characteristic of scheelite from RIRGS and oxidized and reduced skarns (Fig. 7b).

The flat to slightly concave pattern occurs in scheelite from all deposit types (Fig. 7c) and is characterized by La/Sm, Gd/Lu and La/Lu ratios around 1, and with both positive and negative Eu anomalies.

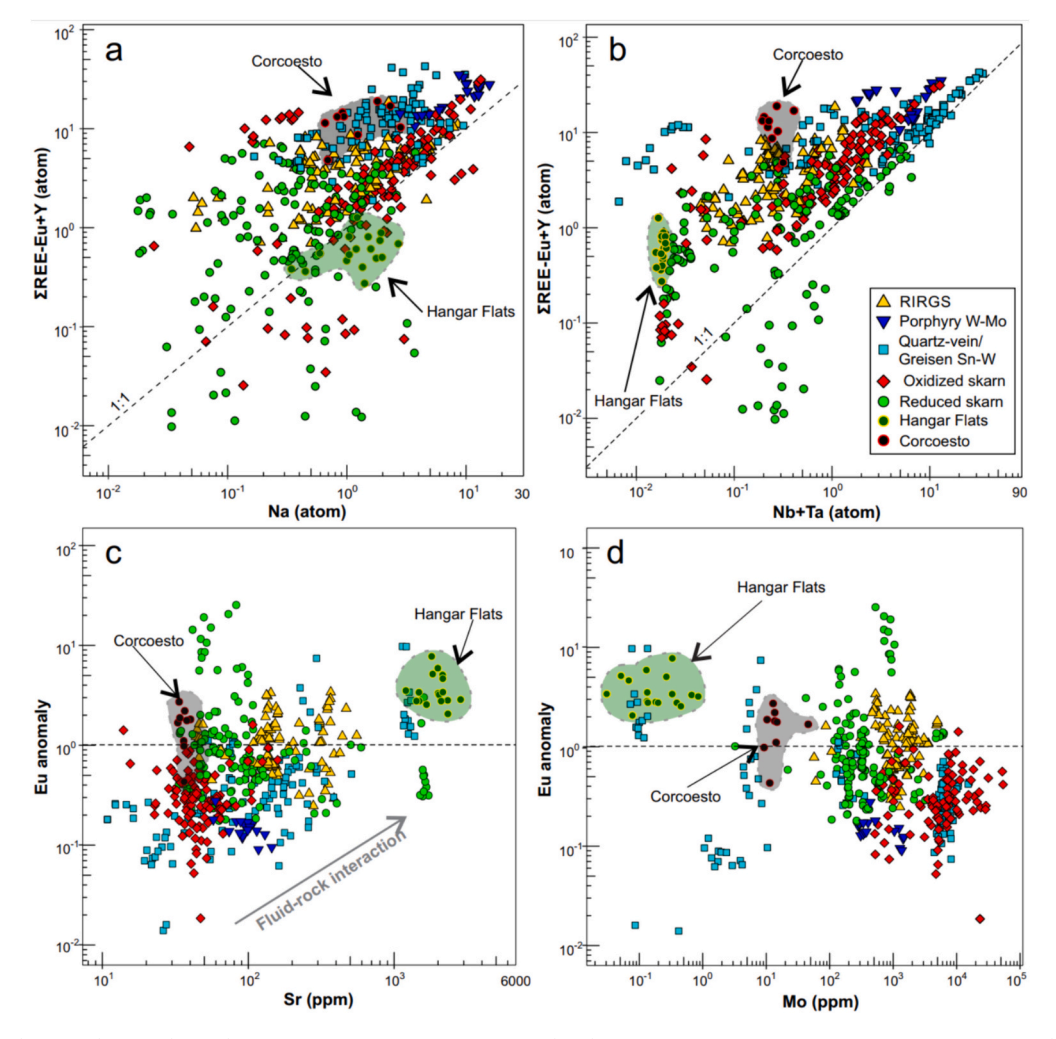


Fig. 5. Binary plot showing the correlation between a. Na versus $\Sigma REE-Eu+Y$; b. Nb + Ta versus $\Sigma REE-Eu+Y$; c. Sr versus Eu anomaly and d. Mo versus Eu anomaly.

Scheelite with this pattern displays slight enrichments in middle REE (Sm—Dy), and in the heavy REE (Ho-Lu; ESM Fig. A1). Few reduced skarn scheelites have ΣREE contents (between 0.8 and 4 ppm) depleted relative to chondrite (Fig. 7c). The concave shape pattern is characterized by La/Sm <1, Gd/Lu >1 and La/Lu from around 1 to higher than 10, and positive to negative Eu anomalies. The concave shape is found in scheelite from all deposit types apart from porphyry W—Mo deposits (Fig. 7d). The convex REE pattern displays La/Sm >0.7 and Gd/Lu <1 ratios, with positive or negative Eu anomalies, mostly in scheelite from quartz-vein/greisen Sn—W, with a few from reduced and oxidized skarns (Fig. 7e).

The positive slope REE patterns are characterized by La/Sm, Gd/Lu and La/Lu ratios <1, predominantly negative Eu anomalies and are mostly in scheelite from quartz veins/greisen-type W—Sn deposit, with few from oxidized skarn and RIRGS (Figs. 7f; ESM Fig. A1).

5. Multivariate statistical analysis of scheelite composition

5.1. PLS-DA of scheelite from magmatic-hydrothermal deposits

Fig. 8 displays PLS-DA results of compositional variation of scheelite from magmatic-hydrothermal deposits: RIRGS, porphyry W—Mo, quartz-veins/greisen Sn—W and oxidized and reduced skarns. The loadings plot of the first and second (qw*1-qw*2) components shows the relationship between the variables (Na, Mg, K, Ti, V, Mn, As, Sr, Y, Nb, Mo, Ta, Pb, Th, U, EREE and Europium anomaly) and the groups

(Fig. 8a), whereas the scores plot displays the distribution of samples in t1-t2 space (Fig. 8b). Positive correlations exist between As and V at negative qw*1 and positive qw*2; Pb, Y, Th, U, Ta at positive qw*1 and qw*2; and between Mn and Nb at positive qw*1 and negative qw*2 (Fig. 8a).

Fig. 8a show that oxidized skarn plots at negative qw1 and positive qw2 as result of Mo, V and As contributions. Reduced intrusion related gold system plots close to the origin at negative qw*1 and qw*2. Quartz-vein/greisen Sn—W and porphyry W—Mo plot at positive qw*1 and qw*2 as result of As, U, Pb, Th contributions. Reduced skarn plots at positive qw*1 and negative qw*2 as result of Mn and Eu anomaly contributions.

Scheelite from oxidized skarns and RIRGS plot mostly at negative t1, and scatter through positive and negative t2 due to high As, V and Mo contents (Figs. 8b and ESM Fig. A2). Scheelite from porphyry W—Mo plots mostly at positive t1 and t2 as a result of high concentrations of As, Ta, Pb, Th and U (Figs. 8b and ESM Fig. A2), whereas few samples scatter at negative t1 (Fig. 8b). Quartz vein/greisen Sn—W scheelite plots mostly at positive t1, and spreads through negative and positive t2 due to high As, U, Th, Ta and Pb contents (ESM Fig. A2), except for a group of analyses that plot separately at negative t1 and positive t2 because of high As concentrations (Fig. 8b). Scheelite from reduced skarns scatters mostly through negative and positive t1 and negative t2 due to high Nb and Mn concentrations and Eu anomaly, with few analyses in positive t1 and t2 quadrant. The VIP plot (Fig. 8c) highlights that V, Mn, As, Y, Nb, Mo, U and Eu anomaly are important elements (VIP >1) that contribute

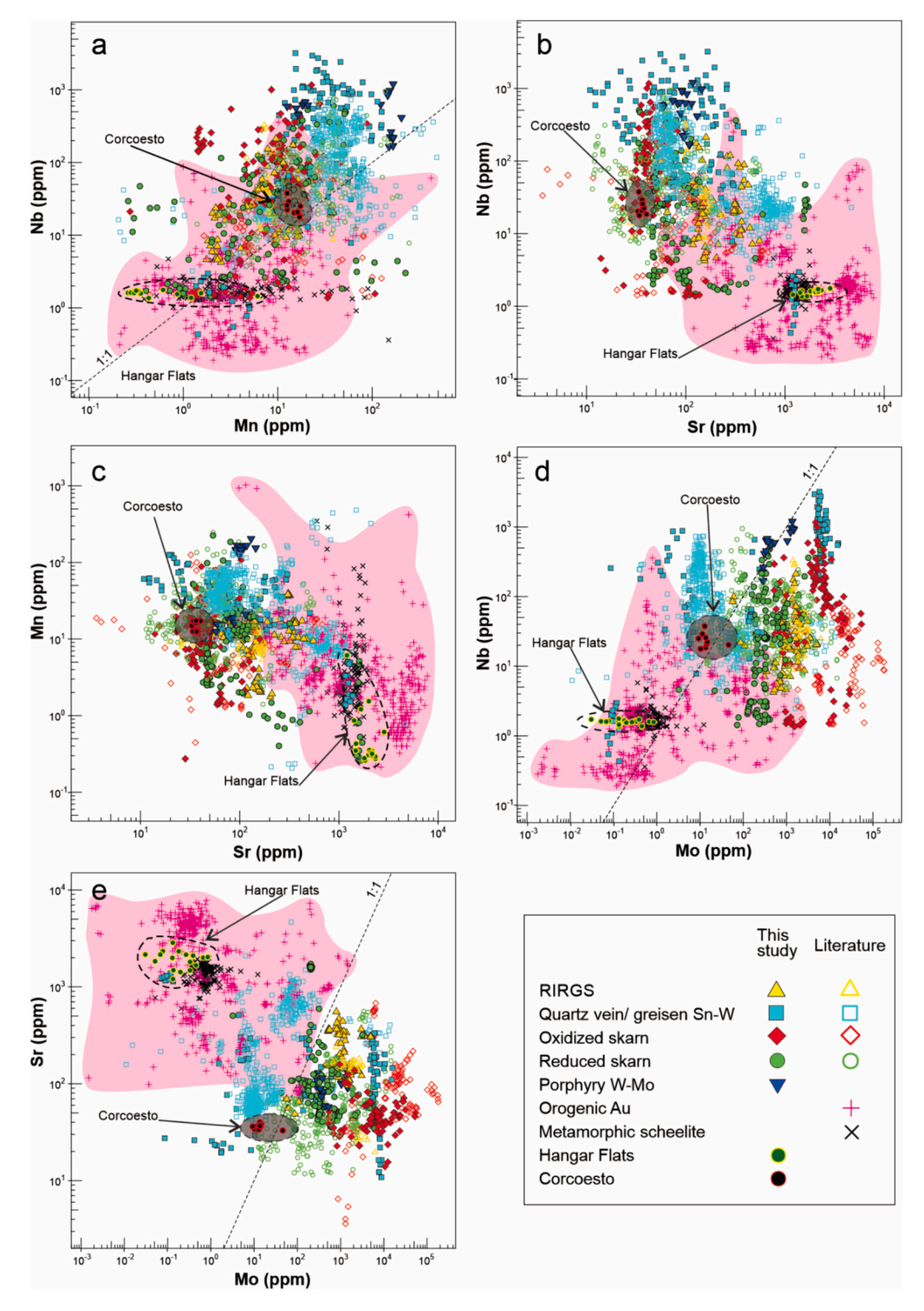


Fig. 6. Binary plots of minor and trace elements composition scheelite. a. Mn versus Nb, b. Sr versus Nb, c. Sr versus Mn, d. Mo versus Nb, and e. Mo versus Sr. Data from this study and literature (Scanlan et al. 2018; De Bronac and de Vazelhes, 2019; Li et al., 2021; Palmer, 2021; Sciuba et al., 2020; Miranda et al., 2022; Pasava unpubl.).

the model, whereas Ti has a moderate contribution (VIP between 0.8 and 1).

5.2. PLS-DA of scheelite-bearing samples from magmatic- and metamorphic-hydrothermal settings

Fig. 9 displays PLS-DA results of compositional variation of scheelite from magmatic- and metamorphic-hydrothermal settings. The loadings

plots of the first and second (qw*1-qw*2; Fig. 9a), and first and third (qw*1-qw*3; Fig. 9c) components show the relationship between the variables (Na, Mg, Mn, As, Sr, Y, Nb, Mo, Pb, ΣREE and Europium anomaly) and the groups, whereas the scores plot displays the distribution of samples in t1-t2 (Fig. 9b) and t1-t3 (Fig. 9d) spaces. Positive correlations exist between Nb and Mn at positive qw*1 and qw*2, Eu anomaly and Sr at negative qw*1 and qw*2, Na, Y and REE at negative qw*1 and positive qw*2 (Fig. 9a), and between As, Pb and ΣREE at

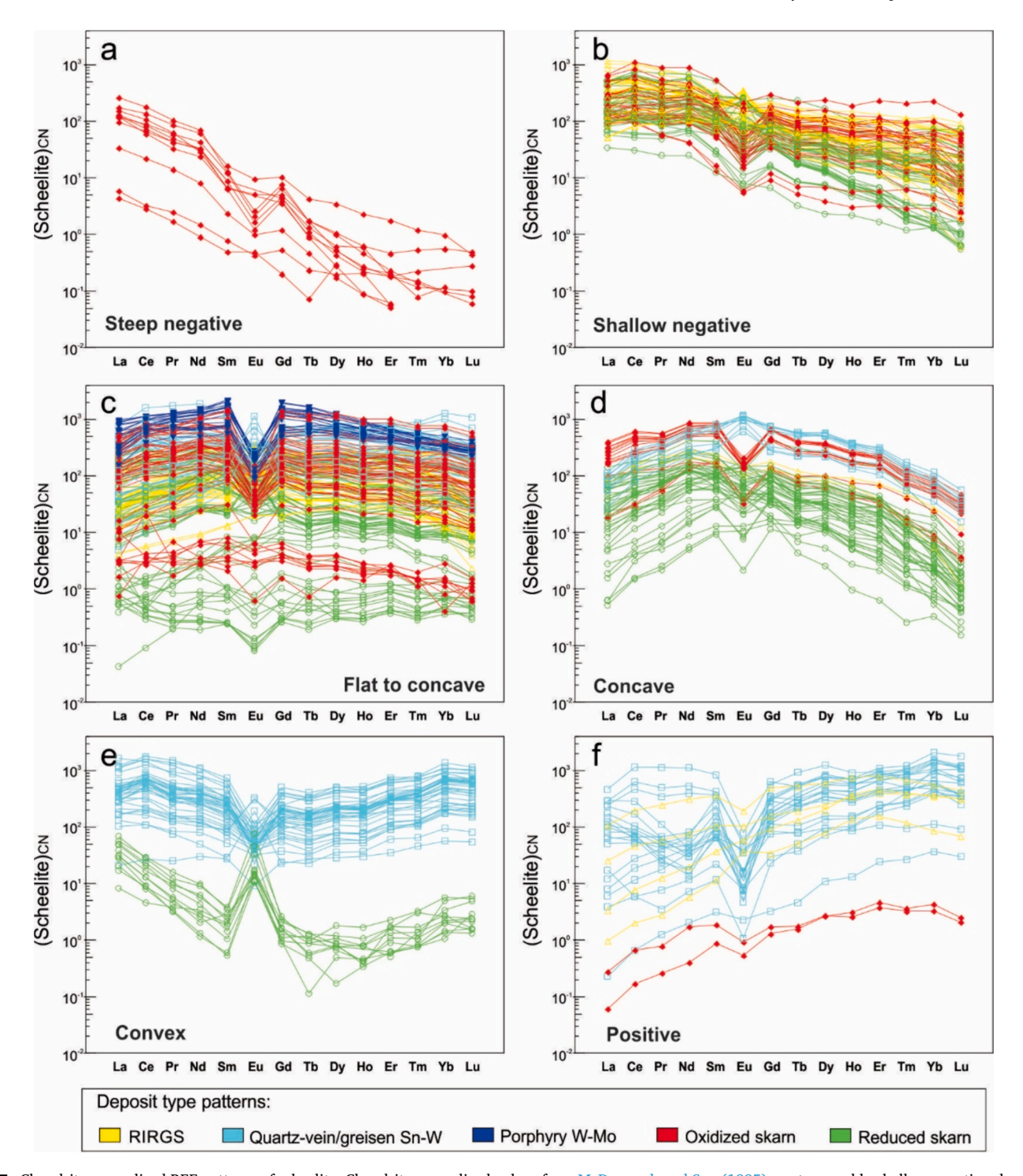


Fig. 7. Chondrite-normalized REE patterns of scheelite. Chondrite normalized values from McDonough and Sun (1995). a. steep and b. shallow negative slope REE patterns in scheelite with predominantly negative Eu anomaly. c. Flat to slightly concave shape with positive and negative Eu anomalies. Note that few reduced skarn scheelite are depleted in REE and display scheelite/chondrite ratio < 1. d. concave REE patterns with predominantly negative Eu anomaly. e. convex shape with both positive and negative Eu anomalies, and f. positive slope with negative Eu anomaly.

negative qw*1 and positive qw*3 (Fig. 9c). Additionally, scheelite from Corcoesto and Hangar Flats are plotted in the PLS-DA model to compare their chemical affinity to scheelite from diverse deposit types (Fig. 9b,d).

Fig. 9a shows that reduced and oxidized skarns and RIRGS plot at positive qw*1 and negative qw*2 as result of Mo contribution. Quartz-vein/greisen Sn—W and porphyry W—Mo plot at positive qw*1 and qw*2 as result of Nb, Mn, Y and Σ REE contributions. Metamorphic scheelite plots at negative qw*1 and qw*2 related to Eu anomaly and Sr contributions, and orogenic Au scheelite plots at negtive qw*1 and

positive qw*2 as result of Sr and Y contributions. Overall, orogenic Au and metamorphic scheelite are mainly discriminated from quartz-vein/greisen Sn—W, porphyry W—Mo, RIRGS and reduced and oxidized skarns by qw*1, due to negative correlation between Sr with Mo and Mn, whereas oxidized and reduced skarns, and RIRGS are mainly discriminated from porphyry W—Mo and quartz-vein/greisen Sn—W by qw*2.

Fig. 9b shows significant overlaps between orogenic Au and metamorphic scheelite, and between orogenic Au and quartz-vein/greisen Sn—W scheelite at negative t1 and positive and negative t2. Few

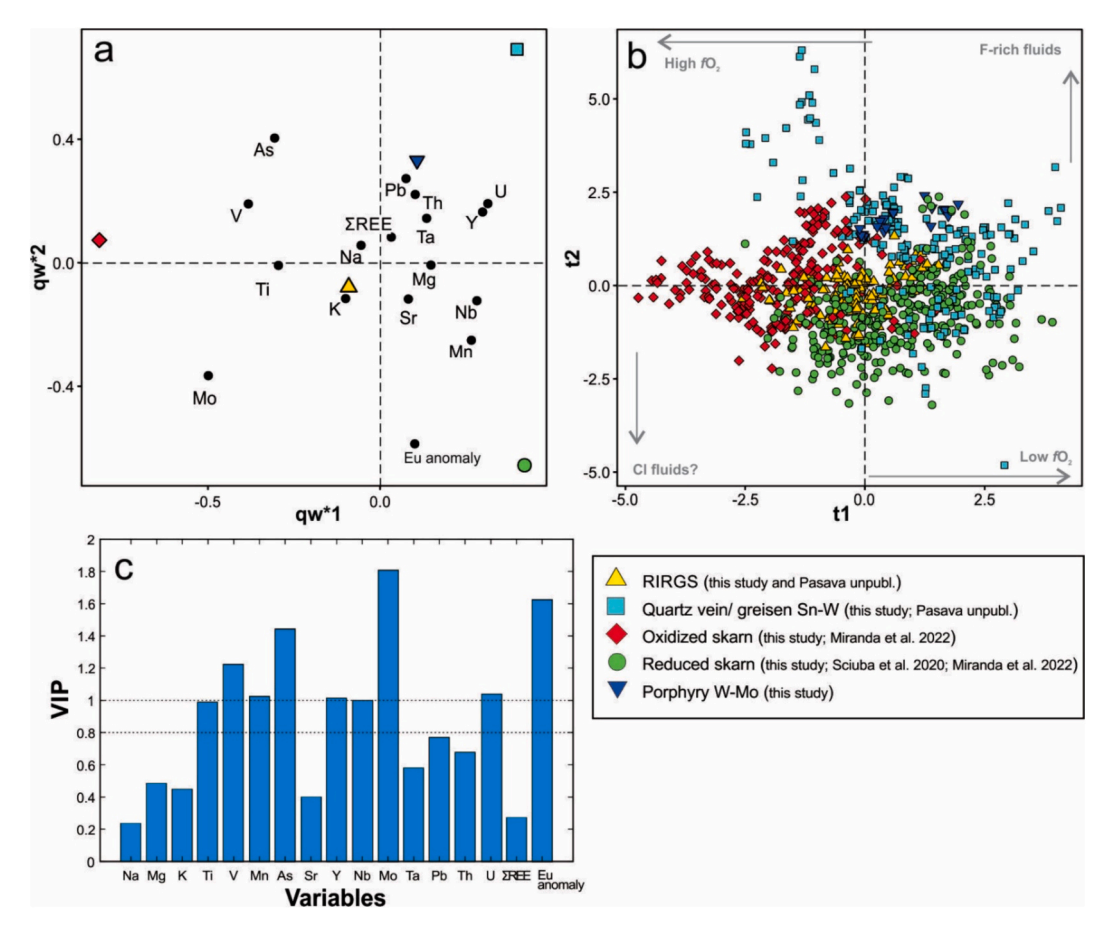


Fig. 8. Partial least-squares discriminant analysis (PLS-DA) of LA-ICP-MS data for scheelite from magmatic-hydrothermal deposits. a. qw^*1-qw^*2 (first and second loadings) plot showing the correlations among elemental variables and magmatic-hydrothermal deposit types. b. t1-t2 (first and second scores) plot showing the distribution of scheelite analyses in the latent variable space defined by qw^*1-qw^*2 . c. Variable Importance on Projection (VIP) plot showing the importance of compositional variables in the PLS-DA model.

analyses of quartz-vein/greisen Sn—W scheelite spread through all the quadrants, but most of them cluster through negative and positive t1 and positive t2. Porphyry W—Mo scheelite clusters at positive t1 and t2, overlapping with few scheelite from reduced and oxidized skarns and from quartz-vein/greisen Sn—W. Oxidized skarn scheelite plots mostly at positive t1 and negative t2 due to high Mo concentrations, with few analyses at positive t2 as result of high Nb and Mn contents. Corcoesto scheelite plots at positive t1 and t2, overlapping with the cluster of quartz-vein/greisen Sn—W scheelite. Hangar Flats scheelite plots mostly at negative t1 and t2, which coincide with the orogenic Au field and metamorphic scheelite.

In the qw*1-qw*3 plot (Fig. 9c), metamorphic scheelite plots at negative qw*1 and qw*3 as result of Eu anomaly, Na and Mg correlations, whereas orogenic Au plot at positive qw*3 due to correlations among Pb, As and SREE. Porphyry W-Mo, reduced skarn and quartzvein/greisen plot at negative qw*3, whereas oxidized skarn and RIRGS plot at positive qw*3. In the space t1-t3 (Fig. 9d), scheelite from all magmatic-hydrothermal deposits overlap each other mostly at positive t1 and positive and negative t3. In contrast, metamorphic scheelite clusters at negative t1 and t3 as result of high Mg and Na contents, whereas orogenic Au scheelite plot mostly at negative t1 and positive t3 with few analyses at negative t3 (Fig. 9d). Similar to t1-t2 space, in t1-t3 space Corcoesto scheelite plots closely to scheelite from magmatichydrothermal deposits, whereas Hangar Flats scheelite plots between the clusters of metamorphic and orogenic Au scheelite. Overall, Sr, Y, Nb, Mo and Eu anomaly are the most important for the discrimination (VIP > 1), followed by Na, Mn, As and Σ REE, with moderate importance (VIP > 0.8) (Fig. 9e).

5.3. Random Forest

The RF classification was performed using only scheelite-bearing deposit types (i.e., RIRGS, reduced and oxidized skarns, quartz vein/greisen Sn—W, porphyry W—Mo and orogenic Au deposits). Metamorphic scheelite was not used in the classifier since it is not a type of deposit, and because all analyses are from the same site (Boanerges Peak). However, it was used as blind data in testing the RF classifier. Therefore, using 70 % of the untransformed data to train the RF classifier, 11 variables and 6 deposit classes, RF classifier yields an overall prediction accuracy of 97 %. Testing data outcome is summarized in the Table 3 and the variable importance shown in the Fig. 10.

Molybdenum, Nb, Sr, Y, Pb and As have the highest mean decrease Gini score followed by Mn, Na and Σ REE. Europium anomaly and Mg display the lowest scores (Fig. 10). The confusion matrix (Table 3) shows accuracies higher than 89 % for all deposit types, where 89.2 % of RIRGS, 100 % of porphyry W—Mo, 97.8 % of quartz-veins/greisen Sn—W, 96.9 % of oxidized skarns, 98.1 % of reduced skarns and 99.3 % of orogenic Au of the test data were correctly classified. The highest misclassified prediction was for RIRGS, where approximately 8 % of the test data were classified as reduced skarn, and 3 % as quartz-veins/greisen Sn—W. All the other misclassifications yield below 3 % (Table 3).

Fig. 11 and Tables 4 and 5 show the prediction results for the scheelite from Hangar Flats and Corcoesto and for blind data, which includes scheelite from orogenic Au (Cave, 2016; Cave et al., 2017; Liu et al., 2021) and W greisen and oxidized skarn deposits (Huang et al., 2022), and metamorphic scheelite (Cave et al., 2017; Palmer, 2021). All

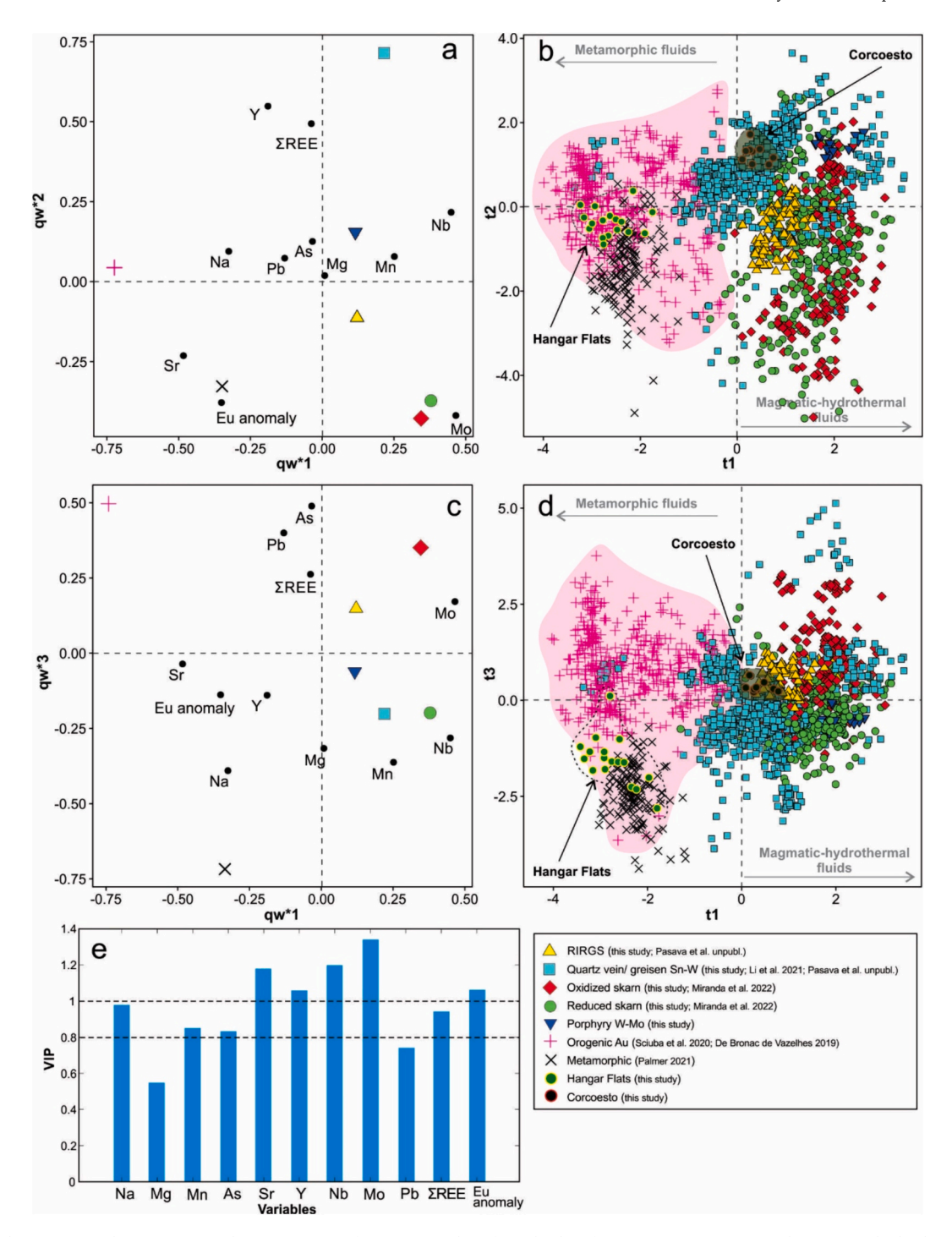


Fig. 9. Partial least-squares discriminant analysis (PLS-DA) of LA-ICP-MS data for scheelite from orogenic settings and magmatic-hydrothermal deposits. a. qw*1-qw*2 (first and second loadings) and c. qw*1-qw*3 (first and third loadings) plots show the correlations among elemental variables and orogenic settings and magmatic-hydrothermal deposit types. b. t1-t2 (first and second scores) and d. t1-t3 (first and third scores) plots show the distribution of scheelite analyses in the latent variable space defined by qw*1-qw*2 and qw*1-qw*3, respectively. e. Variable Importance on Projection (VIP) plot showing the importance of compositional variables in the PLS-DA model.

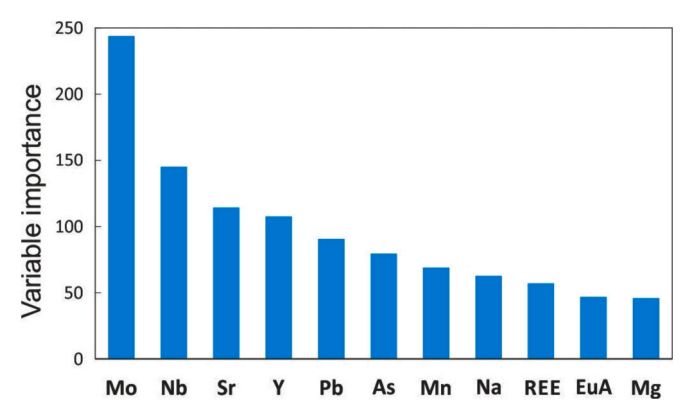
scheelite analyses (100 %) from Hangar Flats, Majiayao and Paradise were correctly predicted as orogenic Au (Tables 4 and 5). Approximately 98 % of scheelite from The Ovens were correctly predicted as orogenic Au and 2 % misclassified as RIRGS, whereas ~63 % of the ones from Mt. Judah scheelite were correctly classified as orogenic Au and 37 % misclassified as RIRGS and reduced skarn (Table 4; Fig. 11). Scheelite from Xiadian displays the smallest percentage of correct predictions, where nearly only 11 % of scheelite analyses were classified as orogenic Au,

and 89 % were misclassified as quartz-vein/greisen Sn—W (Table 4; Fig. 11). On the other hand, scheelite from Corcoesto was predicted mostly as quartz-vein/greisen Sn—W (77 %) and as reduced skarn (23 %) instead of orogenic Au (Fig. 11).

In Weijia greisen- and skarn-type W deposit, 71.4 % of scheelite hosted in quartz-vein/greisen were correctly classified whereas the 28.6 % remaining were misclassified as porphyry W—Mo (Table 4; Fig. 11). Yet for those scheelite hosted in skarns, \sim 91 % were correctly classified

Table 3Confusion matrix of the Random Forest model testing data.

		Predicted									
		RIRGS	Porphyry W- Mo	Quartz-vein/ Greisen W-Sn	Oxidized skarn	Reduced skarn	Orogenic gold	Sum	% correctly classified		
Reference	RIRGS	33		1		3		37	89.2		
	Porphyry W-Mo		6					6	100.0		
	Quartz-vein/Greisen			223		1	4	228	97.8		
	W-Sn										
	Oxidized skarn	1			63	1		65	96.9		
	Reduced skarn				2	101		103	98.1		
	Orogenic gold			1			137	138	99.3		
	0 0							Accuracy	97 %		



 ${\bf Fig.~10.}$ Bar plot showing the variable importance for the RF classification model.

as oxidized skarns and ~ 9 % as porphyry W—Mo, quartz-vein/greisen Sn—W and reduced skarn (Fig. 11; Table 4). Seventy-five percent of Fiddlers Flat, 100 % Lake Hawea and 73 % of Boanerges Peak metamorphic scheelite were predicted as orogenic Au (Table 5). The remaining data was predicted as quartz-vein/greisen Sn—W (Fig. 11).

6. Discussion

6.1. Trace element incorporation and REE patterns

Trace element composition of scheelite depends on fluid and host rock compositions, temperature, pressure, fO_2 , pH, crystallographic control and the partition coefficients between fluid, scheelite, and coprecipitating minerals (Ghaderi et al., 1999; Brugger et al., 2000; Song et al., 2014; Sciuba et al., 2020). Scheelite (CaWO₄) forms a complete solid solution with powellite (CaMoO₄), where Mo⁶⁺ replaces W⁶⁺ at moderate to high fO_2 (Hsu and Galli, 1973; Hsu, 1977; Tyson et al., 1988). Niobium⁵⁺, Ta⁵⁺, As⁵⁺ and V⁵⁺ are substitute for W⁶⁺ following the substitution described below, whereas divalent cations (Sr²⁺, Eu²⁺, Mn²⁺, Pb²⁺ and Mg²⁺) are readily incorporated into Ca-site due their similarities to Ca²⁺.

Additionally, scheelite contains significant amounts of ΣREE^{3+} and Y^{3+} that are substitute for Ca^{2+} through three main mechanisms (Nassau, 1963; Burt, 1989; Ghaderi et al., 1999):

(1)
$$2Ca^{2+} = Na^+ + (REE, Y)^{3+}$$

(2)
$$W^{6+} + Ca^{2+} = (Nb, Ta, As, V)^{5+} + (REE, Y)^{3+}$$

(3)
$$3Ca^{2+} = 2(REE, Y)^{3+} + \square Ca$$
, where $\square Ca$ is a vacancy site.

Ghaderi et al. (1999) suggested that the different mechanisms of Σ REE-Y substitution would lead to distinct REE patterns in scheelite: In

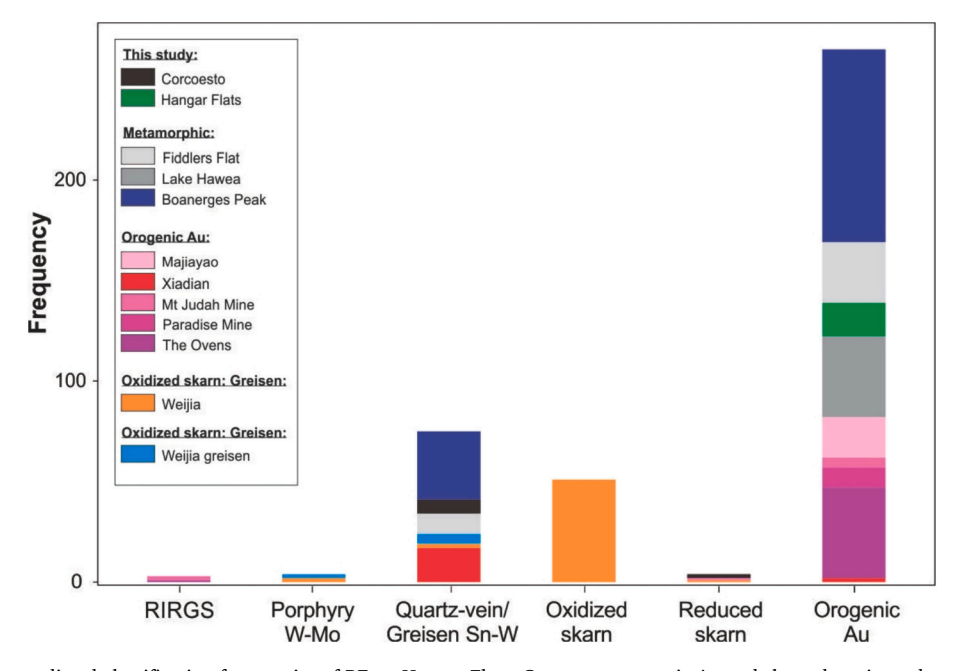


Fig. 11. Histogram of the predicted classification frequencies of RF on Hangar Flats, Corcoesto, orogenic Au and skarn deposits and metamorphic scheelite. (References in ESM Table A5).

Table 4
Proportions of RF classification model predictions for scheelite from orogenic Au deposits and W greisen and skarn. The overall accuracy counts the predictions of orogenic Au and Weijia deposits.

Name	Deposit type	% Correct	Number correctly classified	Number misclassified	Total of analysis
Majiaxao	Orogenic Au	100	20	0	20
Xidian	Orogenic Au	10.5	2	17	19
Mt. Judah	Orogenic Au-W	62.5	5	3	8
Paradise	Orogenic Au	100	10	0	10
The Ovens	Orogenic Au	97.8	45	1	46
	Total Orogenic Au	74.2			
Weijia	Quartz-vein/Greisen	71.4	5	2	7
	Oxidized skarn	91.1	51	5	56
	Overall accuracy	78.9			

Table 5Proportions of RF classification model predictions for scheelite from Corcoesto, Hangar Flats, Fiddlers Flat, Lake Hawea and Boanerges Peak.

Name	Deposit type	% Correct	Number correctly classified	Number misclassified	Total of analysis
Corcoesto	Orogenic Au	0	0	9	9
Hangar Flats	Orogenic Au	100	17	0	17
Fiddlers Flat	Metamorphic	75*	30	10	40
Lake Hawea	Metamorphic	100*	40	0	40
Boanerges Peak	Metamorphic	73.8*	96	34	130
Overall prediction f	for metamorphic scheelite only	83			

eq. (1) for example, Na provides charge balance to maintain crystal neutrality and Na content should be equal to that of Σ REE and Y. As result, because of Ca-site size restrictions, the MREE would be preferentially incorporated into scheelite, resulting thus in a concave REE pattern. Brugger et al. (2000) questioned this statement and showed that even at low Na content, a simple positive correlation between Na and REE—Y, should be necessary to explain the REE-Y incorporation. Our results show that although Na content is lower than that of Σ REE-Eu + Y (Fig. 5a), their positive correlation suggests that REE-Y are partially incorporated by Na charge balance. In addition, we did not notice a direct relation between the concave REE pattern and the Na concentration of scheelite predicted if only eq. (1) accounts for the REE content of scheelite.

The correlation between Nb + Ta versus Σ REE-Eu + Y (Fig. 5b) supports that REE-Y incorporation is also partially governed by eq. (2), because scheelite from all deposit types show strong positive correlation between Nb—Ta and Σ REE-Y (r² = 0.75 and 0.92; Fig. 5b). Additionally, given that few scheelites contain higher Σ REE-Y contents relative to Nb—Ta, at least part of the REE-Y substitution should be controlled by eq. (3).

ESM Fig. A1 shows that scheelite from Mawchi, Felbertal, Obří důl, Dublin Gulch and Čelina deposits display shallow negative slope and flat to concave REE patterns that are similar to that of the felsic intrusions related to the mineralization, suggesting that the exsolved mineralizing fluid REE patterns is controlled by the chemistry of the ore-related intrusions and reflected by the REE concentration of scheelite grains. This supports that scheelite REE patterns are, at least for some case, directly controlled by fluid chemistry regardless of the substitution mechanism controlling the REE incorporation in scheelite.

More fractionated REE patterns such as steep negative slope (Obří důl; ESM Fig. A1), positive (Felbertal; ESM Fig. A1) and convex shapes (Traversella; ESM Fig. A1) or those that differ from the REE pattern of the magmatic source (Nui Phao and Northern Dancer; ESM Fig. A1) suggest that the fluid REE pattern do not always reflect the one of its magmatic source and that other processes (i.e., co-precipitation of other mineral phase, type of ligands, salinity) affect the REE pattern of formed scheelite (Haas et al., 1995; Brugger et al., 2000; Migdisov et al., 2016; Miranda et al., 2022).

Miranda et al. (2022) showed that steep negative slope REE pattern is strongly associated with prograde scheelite from oxidized skarns

compared to reduced skarns. This has been interpreted to be linked to the high-salinity fluids involved in the formation of the prograde scheelite as high Cl concentration favor the transport of LREE over HREE in mineralizing fluid (Haas et al., 1995; Migdisov et al., 2016). Although there is no available information about fluid salinity of the oxidized skarns studied here, we suggest that the similar HREE depletion observed in scheelite from oxidized skarns can result of the same mechanism.

Additionally, Miranda et al. (2022) also pointed out that shallow negative slope REE pattern with a marked depletion between Dy—Lu results from clinopyroxene co-precipitation, which leads to a depletion of Dy—Lu in the fluid. Brugger et al. (2000) emphasized that the occurrence of MREE-depleted/convex REE pattern in scheelite would be explained by scheelite precipitation itself in a closed-system, which preferentially incorporates MREE over LREE and HREE (Li et al. 2018; Poulin et al. 2018). A similar argument is presented by Cave et al. (2017) for scheelite from quartz-vein and metasedimentary rocks in the Otago Schist, which display positive slope REE pattern (Palmer, 2021). Therefore, the occurrence of fractionated REE patterns such as convex shape and positive slope REE patterns likely results from the coprecipitation of REE-bearing minerals, during the evolution of hydrothermal systems.

6.2. Eu anomaly

Similar to REE patterns, the Eu anomaly in scheelite is often interpreted as inherited from the mineralizing fluid and reflects the fluids source (Ghaderi et al., 1999; Song et al., 2014). Magmatic-derived fluids commonly display negative Eu anomaly as a result of plagioclase crystallization in their magmatic source rocks (Banks et al., 1994; Baker et al., 2004). As shown in ESM Fig. A1, scheelite displays similar Eu anomaly, as well as REE patterns, to that of the related intrusion (Mawchi, Felbertal, Obří důl, Traversella, Dublin Gulch, Čelina and Northern Dancer), suggesting that in part, scheelite Eu anomaly is inherited from the fluid source. However, few scheelites from reduced skarns, RIRGS and quartz-vein/greisen yield weak to strong positive Eu anomalies (Fig. 5c; ESM Fig. A1), implying that factors such as temperature, pH, and fO_2 of the hydrothermal fluids, as well as the breakdown of Ca-bearing minerals (e.g., plagioclase) during fluid-rock interaction control Eu²⁺/Eu³⁺ ratio of the fluids, and consequently the

Eu anomalies of scheelite (Bau, 1991; Ghaderi et al., 1999; Brugger et al., 2000, 2008; Song et al., 2014; Sun and Chen, 2017; Sun et al., 2019; Wu et al., 2019; Yuan et al., 2019).

An accurate estimation of the importance of the different factors influencing the Eu anomalies of scheelite is challenging given that we do not have detailed information about fluid composition of the studied samples. However, correlations among Eu anomaly, Sr and Mo, and the REE patterns may suggest that fluid-rock interaction and fO₂ have a control on the Eu anomaly (Brugger et al., 2000, 2008; Song et al., 2014). Previous studies have shown that the breakdown of Ca-bearing minerals, such as plagioclase to form mica during fluid-rock interaction, releases Eu and Sr into the fluid (Sverjensky, 1984; Yuan et al., 2019). So, a progressive increase of Sr contents coupled with smaller negative Eu anomalies in scheelite may be a result of the progressive breakdown of plagioclase during alteration. The positive relationship between Eu anomaly and Sr in scheelite from quartz-vein/greisen Sn—W deposits where there is a strong feldspar-destructive phyllic alteration supports this hypothesis (Fig. 5c). On the other hand, the same does not occur in few scheelites from reduced skarns and RIRGS (Fig. 5c).

Molybdenum content in scheelite is often used as a proxy of fO_2 (Hsu and Galli, 1973; Hsu, 1977). Under reduced conditions Mo occurs as Mo⁴⁺ and is not compatible in the scheelite structure, whereas under more oxidized (high oxygen fugacity) conditions Mo occurs as Mo⁶⁺ and substitutes for W⁶⁺. In addition, sulfur fugacity also influences the incorporation of Mo in scheelite, as for a fixed oxygen fugacity an increase of S fugacity favors the incorporation of Mo in molybdenite (MoS₂; Hsu, 1977). The oxygen and sulfur fugacities of mineralizing fluids from most magmatic-hydrothermal systems are correlated (Einaudi et al., 2003). Therefore, the observed higher Mo content in oxidized skarn characterized by higher S fugacity (pyrite dominated) versus reduced skarn characterized by low S fugacity (pyrrhotite dominated), suggest that oxygen fugacity has more important effect than sulfur fugacity on the incorporation of Mo in scheelite.

As result, low Mo concentrations in scheelite reflects reduced conditions, whereas high Mo content reflects more oxidized conditions (Song et al., 2014; Poulin et al. 2018; Miranda et al., 2022). Therefore, the combination of both Eu anomaly and Mo can provide clues about the redox conditions in the scheelite-related mineralizing systems. Fig. 5d shows decreasing Mo content with increasing positive Eu anomalies in scheelite from RIRGS and for few reduced skarns, which might suggest that reduced condition favor positive Eu anomalies in scheelite. Additionally, few scheelite from quartz-vein/greisen Sn—W deposits with positive Eu anomalies contains very low contents of Mo (<10 ppm), suggesting low fO_2 in the fluids as well.

6.3. Chemical variation in scheelite from distinct magmatic-hydrothermal deposit types

Fig. 8 shows that despite overlaps, scheelite composition varies as function of the magmatic-hydrothermal deposit types and that Ti, V, Mn, As, Y, Nb, Mo, U and Eu anomaly are the most important variables for discrimination (Fig. 8c). This suggests that hydrothermal processes, host rock composition and physico-chemical conditions of the mineralizing fluids typical of the different deposit types control the incorporation of Ti, V, Mn, As, Y, Nb, Mo and U in scheelite. On the other hand, Na, Mg, K, Sr, Ta, Pb, Th and REE are apparently less important variables for deposit type discrimination (Fig. 8c), suggesting that the occurrence of these elements in scheelite was controlled by similar parameters in the different deposit types. Given that in all deposits scheelite precipitated from magmatic-related fluids, those elements are probably reflecting the source of the fluids instead of external variations and physico-chemical conditions triggering scheelite precipitation.

Tungsten mineralization is typically associated with fractionated felsic magmas that form under slightly oxidized to reduced fO_2 conditions (Newberry and Swanson, 1986; Candela, 1992; Wood and Samson, 2000). Miranda et al. (2022) showed that scheelite from oxidized skarns

distinguished from that of reduced skarns based on high Mo, As and V concentrations as a result of oxidized magmatic-derived fluids. In contrast, scheelite from reduced skarns is characterized by low Mo, As and V, and high Mn and Nb contents due to reduced conditions and the availability of these elements in the mineralizing fluids. Thus, the chemical signature of scheelite seems to have a potential to trace the oxygen fugacity of the ore-related intrusions. In fact, the PLS-DA results show that oxidized skarns have high Mo, As and V concentrations (Fig. 8a), implying that scheelite was formed under high fO₂. In contrast, quartz-vein/greisen Sn-W and reduced skarns plot at the right side of the diagram as a result of high Mn and Nb contents, indicating low fO₂, which agrees with the oxidation state of the ore-related intrusions (references in Tables 1 and ESM Fig. A1). Additionally, RIRGS and porphyry W-Mo deposits plot between these two end-members, suggesting thus intermediate fO₂ conditions of the source intrusion relative to reduced and oxidized skarns related intrusions. Therefore, qw*1 separates scheelite-bearing deposit types as a function of the oxidation state of their ore-related intrusions.

Porphyry W-Mo and quartz-vein/greisen Sn-W are characterized by high Th, U, Ta, Y and Pb contents, which discriminate them from oxidized skarns and RIRGS (Figs. 4, 8, and ESM A2). The high concentrations of Th, U, Ta, Y and Pb in scheelite is likely related to the high content of fluorine in the mineralizing fluids common in quartz-vein/ greisen Sn-W deposits (Pollard et al., 1987; Breiter et al., 2017a, b; Song et al., 2014; Pan et al., 2019; Wang et al., 2021). It has been demonstrated that fluorine increases the solubility of REE, Y and HSFE in magma (Keppler, 1993; Agangi et al., 2010). As a result, REE-, Y- and HSFE-rich fluids exsolved from those intrusions can precipitate minerals that having high REE, Y, Pb, Nb, Ta, U and Th concentrations, such as scheelite. The occurrence of abundant fluorite in scheelite-bearing samples from porphyry W-Mo and quartz-vein/greisen Sn-W deposits support this hypothesis (Table 1). Even if our data show an influence of fluid composition (inherited from the source intrusions) on the chemical composition of scheelite, it has been showed that scheelite composition is also affected by the nature of the wall rock (Scanlan et al., 2018; Sciuba et al., 2020; Palmer et al., 2022). Several studies have demonstrated that the fluid-rock interaction and fluid mixing are important for the precipitation W-bearing minerals (Lecumberri-Sanchez et al., 2017; Legros et al., 2020; Liu et al., 2022), besides of being common processes in magmatic-hydrothermal systems (Audétat and Edmonds, 2020). Heterogeneous Sr isotope ratios in a single scheelite grain from magmatic-hydrothermal systems reflect change from a Sr magmatic to wall rock Sr source (Kozlik et al., 2016a, b; Liu et al., 2022). Similarly, compositional maps of scheelite associated with reduced skarns at the Cantung W deposit (Canada) show an increase of Sr content towards the rim (Miranda et al., 2022). These findings corroborate for the influence of the host rock composition in the scheelite trace element distribution.

6.4. Chemical variations in scheelite from distinct fluid sources: magmatic vs metamorphic

Orogenic Au deposits and metamorphic scheelite are characterized by low Mo, Nb and Mn, high Sr and Na contents, with commonly positive Eu anomalies (Figs. 6 and 9). In contrast, scheelite from magmatichydrothermal settings have higher Mo, Nb and Mn, lower Sr and Na contents, and both negative and positive Eu anomalies (Figs. 6 and 9). The distinct contents of these elements in scheelite are mainly a function of fluid source (magmatic vs metamorphic), host rocks and of the physico-chemical conditions inherent to each deposit type, supporting thus the use of scheelite composition as a fluid-source tracker (Fig. 9). It is noteworthy to point that although RIRGS and orogenic Au deposits share several similar features such as low salinity, CO₂-rich and reduced fluids and anomalous Te, W and Bi signature (Baker, 2002; Goldfarb et al., 2005; Hart, 2007), our results show that scheelite associated with RIRGS is chemically distinct to those from orogenic Au deposits

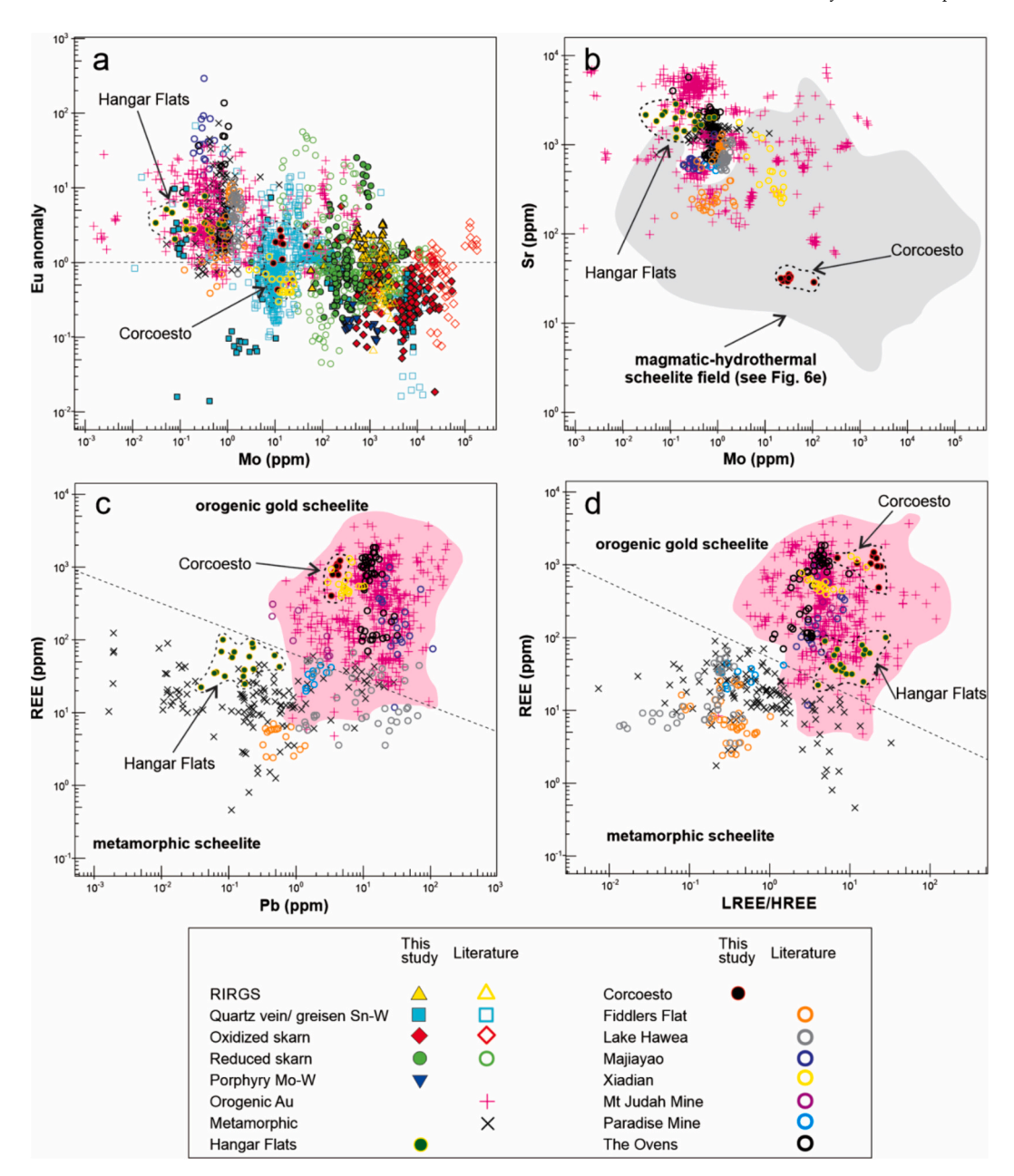


Fig. 12. Binary plot showing in a. Mo versus Eu anomaly and b. Mo versus Sr for scheelite from magmatic-hydrothermal and orogenic settings, and in c. Pb versus REE and d. LREE/HREE versus REE for scheelite from orogenic settings only (orogenic gold and metamorphic scheelite). Data from this study and literature, references in ESM Tables A6 and A7. (For interpretation of the references to color in this figure legend, the reader is referred to the web version of this article.)

characterized by the higher Mo, Nb and Mn contents (Fig. 9b), consistent with the distinct fluid sources for both deposit types.

The low Mo content (<100 ppm) and characteristic positive Eu anomaly displayed by scheelite from orogenic settings (Fig. 12a) support a relatively reduced metamorphic-derived fluids relative to magmatic-derived fluids, which are more oxidized (Song et al., 2014; Poulin et al. 2018; Sciuba et al., 2020). The high Sr content in metamorphic and orogenic Au scheelite results from the release of Sr during the break-down of Ca-bearing minerals hosted in metasediments and/or maficultramafic volcanic rocks (Paterson and Rankin, 1979; Kempe et al., 2001), whereas the low concentrations of Nb and Mn are linked to their low concentration in the host rocks (Sciuba et al., 2020). In contrast, the low content of Sr from exsolved magmatic-derived fluids that are depleted in Sr due to plagioclase crystallization during differentiation of their source magmas (Miller and Mittlefehldt, 1984), whereas Nb and

Mn have an incompatible behavior relative to Sr, thus becoming enriched in the magma during fractional crystallization, and consequently become concentrated in the mineralizing fluid compared to metamorphic fluids (Figs. 6a-c; Miller and Stoddard, 1981; Sha and Chappell, 1999; Piccoli and Candela, 2002; Seo et al., 2020). As a result, scheelite from magmatic-hydrothermal settings contains higher Nb and Mn contents relative to those from orogenic settings formed by metamorphic fluids (Figs. 6a, d-e and 9).

Additionally, Fig. 9c-d highlight that metamorphic scheelite contains low ΣREE , As and Pb contents relative to those associated with gold mineralization, thus allowing their discrimination as show Figs. 12c-d. Palmer et al. (2022) pointed out that the low ΣREE , Pb and As contents in metamorphic scheelite from the Otago schist is likely related to local host rock compositions which are poor in these elements, and/or to the low metamorphic conditions (sub- to low-greenschist facies), which do not allow the release these elements from their host minerals (Cave

et al., 2017). Moreover, Sr isotopic ratios reveal that scheelite that is not associated with gold displays a heterogeneous isotopic signature that arises from local variations of the host rocks and small amounts of fluid flow. On the other hand, scheelite that formed temporally and spatially associated with gold displays a homogeneous signature, which results from fluids derived from a distal source with long fluid flow pathway (Scanlan et al. 2018; Palmer et al., 2022).

In summary, metamorphic grade conditions, host rock composition and the transport of fluids along variable pathways are essentials factors controlling gold mineralization in orogenic settings, which are recorded in scheelite chemistry (Cave et al., 2017; Scanlan et al. 2018; Sciuba et al., 2020; Palmer, 2021). The compatibility of Sr and Eu during felsic magma crystallization and the abundance of Mo, Nb and Mn either due to fO_2 or incompatible behavior of these elements during magma crystallization or the local host rock contribute to discriminate scheelite from distinct mineral deposit types (Figs. 6, 8, 9 and 12).

7. Implications for mineral exploration

Previous studies have attempted to use scheelite chemistry to differentiate deposit types through binary diagrams or multivariate methods (Song et al., 2014; Poulin et al. 2018; Sciuba et al., 2020; Miranda et al., 2022). Binary diagrams have become less effective especially for those scheelite that form under similar hydrothermal conditions (i.e., RIRGS vs reduced skarns; Fig. 6). Alternatively, the combination of several variables with supervised classification methods have shown great improvement in the results, allowing a better discrimination among different scheelite-bearing deposits (Figs. 8 and 9), even with limited literature data (Sciuba et al., 2020). Our results show that, although PLS-DA is useful for discrimination and to understand the correlation between variables and samples, there is still a small overlap between scheelite from magmatic-hydrothermal and orogenic settings (Fig. 9).

Recent studies show that the RF classifier is an effective tool for mineral deposit discrimination and prediction (O'Brien et al., 2015; Gregory et al., 2019; Liu and Beaudoin, 2021; Bédard et al., 2022; Nathwani et al., 2022). The high overall accuracy of testing data prediction (97 %) enhances the efficiency of the RF classifier to predict mineral deposit types based on scheelite composition.

Scheelite from Corcoesto Au deposit has similar contents of Mo, Mn and Nb to that of worldwide orogenic Au deposits (Fig. 6), but its low Sr content made it classified as quartz-vein/greisen Sn-W and as reduced skarn in both PLS-DA and RF models, since Sr is an important element for discrimination of scheelite between orogenic gold and magmatichydrothermal deposits (Figs. 9 and 10). Similar to Variscan Au deposits in Western Europe (Castromil, Limarinho and Penedono), the Corcoesto Au deposit is shear-hosted, developed along strike-slip fault systems linked to late stages of the Variscan orogeny (Boiron et al., 2003; Vallance et al., 2003; Fuertes-Fuente et al., 2016; Neiva et al., 2019) and might be associated with greisenisation of the host rocks, a characteristic of quartz-vein/greisen Sn-W deposits (Vallance et al., 2003). In addition, in these deposits Au deposition is linked to mixing between ascending metamorphic fluid with shallow meteoric water (Boiron et al., 2003), and thus the low Sr content of the scheelite may be caused by this input of Sr-poor meteoric water. More studies are needed to confirm this hypothesis. Therefore, these atypical features can partly explain the misclassification of scheelite from Corcoesto Au deposit as reduced skarn or quartz-vein/greisen Sn-W deposits by our PLS-DA and RF models. It is noteworthy that orogenic gold, reduced skarn and vein quartz/greisen Sn-W deposits formed from more reduced fluids, perhaps providing another explanation for the misclassification of Corcoesto.

Hangar Flats scheelite displays chemical similarities to that from orogenic settings (Figs. 9b,d) and is predicted as belong to orogenic Au deposit (Fig. 11), agreeing with the findings of Wintzer et al. (2022), who showed that the W mineralization is no related to magmatic-

hydrothermal fluids. Moreover, our results also show that Hangar Flats scheelite has low Pb, As and REE contents as does metamorphic scheelite (Figs. 4, 6, 9 and 12c). Given the similarity between metamorphic and Hangar Flats scheelite and considering that the W (57 Ma) or W—Sb (45 Ma) mineralization postdates the Au mineralization (67–58 Ma), our results may suggest that Hangar Flats scheelite from the first W mineralization formed from the similar type of metamorphic fluid as the Otago metamorphic scheelite (Figs. 9 and 12).

Most of scheelite analysis from Majiayao, Mt. Judah, Paradise and The Ovens orogenic Au deposits and Weija skarn-type were correctly classified (Table 4; Fig. 11). In contrast, ~11 % of Xiadian scheelite were predicted as orogenic Au, agreeing with literature classification (Li et al., 2021), whereas most of analyses (89 %) were classified as quartz-vein/greisen Sn—W. As shown in Fig. 12a-b, Xiadian scheelite displays intermediate Mo and Sr contents relative to orogenic gold and magmatichydrothermal deposits, with mostly negative Eu anomalies, which make it more similar to scheelite from quartz-vein/greisen Sn—W. According to the authors, the Sr and Pb isotope signatures of scheelite and galena, respectively, at Xiadian revealed mixed reservoir sources originated from the nearby granite and metasediments (Li et al., 2021), which may explain classification as quartz-vein/greisen Sn—W and part of orogenic Au deposits.

Although the RF model does not contain metamorphic scheelite in the classification, the prediction of metamorphic scheelite as from orogenic Au deposits enhances the effectiveness of the RF model to predict scheelite from different geological settings and fluid source (Table 5; Fig. 11). Moreover, the relation between REE and Pb or LREE/HREE is useful to discriminate orogenic Au scheelite from metamorphic scheelite (Fig. 12c,d). Although metamorphic scheelite is not associated with Au (Cave et al., 2017; Scanlan et al. 2018; Palmer, 2021), the occurrence of this type of scheelite in glacial and stream sediments provides evidence of metamorphic terrains that may contains resources of W as is the case of Otago schist, such as Glenorchy (Mutch, 1969; Palmer, 2021).

The efficiency of the RF classifier is limited by the record of the natural variation of scheelite chemistry that can be used to train the model. New scheelite compositional data from various settings will contribute to provide a more comprehensive record of scheelite composition in nature. This will not only increase the knowledge of natural variability of scheelite chemistry but also reduce class imbalance between various settings, which negatively impacts the efficiency of machine learning methods to predict the source of scheelite in less well-characterized scheelite settings.

8. Conclusion

Our study highlights that scheelite composition varies following deposit types and genesis of the hydrothermal fluids, supporting its use as a mineral deposit type discriminator and its application to mineral exploration targeting. Texturally, scheelite varies from fine- to coarsegrained regardless the deposit type. Scheelite from RIRGS is predominantly homogenous under CL images, whereas in the others deposits it varies from homogenous to zoned. Trace element compositions reveal that scheelite display 6 REE patterns with predominantly negative Eu anomaly, which result from different magma composition, salinity and co-genetic REE-bearing minerals. Few scheelite display positive Eu anomalies that is likely due to fluid-rock interaction, and changes in pH, fO2 and temperature. The PLS-DA highlights that scheelite from magmatic-hydrothermal deposits vary in composition as a result of fluid fO2 and composition. The low Sr and Eu content of magmatic-related scheelite due to the compatible behavior of these elements during felsic magma fractionation, and the relative high abundance of Mo, Nb and Mn in magmatic-related scheelite allow to discriminate them from scheelite form by metamorphic fluids in orogenic settings. Metamorphic scheelite with no temporal association with Au contains lower REE, As and Pb contents and LREE/HREE ratio relative to that associated with Au that is likely related to local source for hydrothermal fluids, host rock compositions and low metamorphic grade. Based on the concentrations of Na, Mg, Mn, As, Sr, Y, Nb, Mo, Pb, REE and Eu anomalies in scheelite, a Random Forest classifier yields an overall accuracy of 97 %. Predictions from literature data show the effectiveness of the Random Forest scheelite model in predicting mineral deposit types and geological settings, supporting its application as an effective tool for mineral exploration.

Supplementary data to this article can be found online at https://doi. org/10.1016/j.gexplo.2024.107555.

Funding

This research was supported by the Natural Sciences and Engineering Research Council (NSERC) of Canada, Agnico Eagle Mines Ltd., and Ministère de l'Énergie et des Ressources Naturelles du Québec. It is also a contribution to the RENS project (TAČR SS02030023). We thank M. Palmer and an anonymous referee for their comments that helped improve the paper significantly.

CRediT authorship contribution statement

Ana Carolina R. Miranda: Conceptualization, Writing – original draft, Writing – review & editing, Data curation, Formal analysis, Methodology. Georges Beaudoin: Supervision, Writing – review & editing, Funding acquisition, Methodology, Formal analysis. Bertrand Rottier: Supervision, Writing – review & editing, Formal analysis. Jan Pašava: Writing – review & editing, Formal analysis. Petr Bohdálek: Writing – review & editing. Jan Malec: Writing – review & editing.

Declaration of competing interest

The authors declare that they have no known competing financial interests or personal relationships that could have appeared to influence the work reported in this paper.

Data availability

I have shared my data at the attach file step.

Acknowledgments

We would like to thank David Poole (Kinross Gold Corporation), Lara Lewis (Yukon Geological Survey), Khin Zaw (University of Tasmania), Niki Wintzer (USGS), Christopher Dail (Midas Gold Corporation), Franco Pirajno, Olivier Rabeau (Universite Laval), Karsten Aupers (Wolfram Bergbau und Hütten AG) and František Veselovský (Czech Geological Survey) for providing some of the samples, and Marc Choquette (Université Laval), Dany Savard and Audrey Lavoie (Université du Quebec à Chicoutimi) for their assistance with EPMA and LA-ICP-MS analyses.

References

- Agangi, A., Kamenetsky, V.S., McPhie, J., 2010. The role of fluorine in the concentration and transport of lithophile trace elements in felsic magmas: insights from the Gawler Range Volcanics, South Australia. Chem. Geol. 273, 314–325. https://doi.org/ 10.1016/j.chemgeo.2010.03.008.
- Allegro, G.L., 1987. The Gilmore Dome Tungsten Mineralization, Fairbanks Mining District, Alaska: University of Alaska Fairbanks. M.S. thesis, 150 p., illust., maps, 7 folded maps.
- Andersson, S., Wagner, T., Jonsson, E., Fusswinkel, T., Whitehouse, M., 2019. Apatite as a tracer of the source, chemistry and evolution of ore-forming fluids: the case of the Olserum-Djupedal REE-phosphate mineralisation, SE Sweden. Geochim. Cosmochim. Acta 255. 163–187. https://doi.org/10.1016/j.gca.2019.04.014.
- Audétat, A., Edmonds, M., 2020. Magmatic-Hydrothermal Fluids. Elements 16 (6), 401–406. https://doi.org/10.2138/gselements.16.6.401.

- Auwera, J.V., Andre, L., 1991. Trace elements (REE) and isotopes (O, C, Sr) to characterize the metasomatic fluids sources: evidence from the skarn deposit (Fe, W, Cu) of Traversella (Ivrea, Italy). Contrib. Mineral. Petrol. 106, 325–339.
- Averill, S., 2001. The application of heavy indicator mineralogy in mineral exploration with emphasis on base metal indicators in glaciated metamorphic and plutonic terrains. Geol. Soc. London Spec. Publ. 185, 69–81.
- Averill, S.A., 2011. Viable indicator minerals in surficial sediments for two major base metal deposit types: Ni-Cu-PGE and porphyry Cu. Geoch.: Explo. Envir. Analysis 11, 279–291.
- Baker, T., 2002. Emplacement depth and carbon dioxide-rich fuid inclusions in intrusion-related gold deposits. Econ. Geol. 97, 1111–1117.
- Baker, T., Achterberg, E.V., Ryan, C.G., Lang, J.R., 2004. Composition and evolution of ore fluids in a magmatic-hydrothermal skarn deposit. Geology 32 (2), 117–120.
- Ball, C.W., 1954. The Emerald, Feeney and Dodger tungsten ore-bodies, Salmo, British Columbia, Canada, Econ. Geol. 49, 625–638.
- Ballard, J.R., Palin, M.J., Campbell, I.H., 2002. Relative oxidation states of magmas inferred from Ce(IV)/Ce(III) in zircon: application to porphyry copper deposits of northern Chile. Contrib. Mineral. Petrol. 144, 347–364. https://doi.org/10.1007/ s00410.002.0402.5
- Banks, D.A., Yardley, B.W.D., Campbell, A.R., Jarvis, K.E., 1994. REE composition of an aqueous magmatic fluid: a fluid inclusion study from the Capitan Pluton, New Mexico, U.S.A. Chem. Geol. 113, 259–272. https://doi.org/10.1016/0009-2541(94) 90070-1
- Barnes, S.J., Mansur, E.T., Pagé, P., 2022. Differences in composition of chromites from low-Ti and high-Ti picrites of the Emeishan Large Igneous Province and comparison with chromites of the UG-2 platinum-deposit of the Bushveld complex. Lithos 412, 106613.
- Bau, M., 1991. Rare earth element mobility during hydrothermal and metamorphic fluidrock interaction and the significance of the oxidation state of europium. Chem. Geol. 93, 219–230.
- Bédard, É., Bronac, De, de Vazelhes, V., Beaudoin, G., 2022. Performance of predictive supervised classification models of trace elements in magnetite for mineral exploration. J. Geochem. Explor. 236, 106959 https://doi.org/10.1016/j. gexplo.2022.106959.
- Bell, K., Anglin, C.D., Franklin, J.M., 1989. Sm-Nd and Rb-Sr isotope systematics of scheelites: Possible implications for the age and genesis of vein-hosted gold deposits. Geology 17, 500–504.
- Belousova, E.A., Griffin, W.L., O'Reilly, Y., Fisher, N.I., 2002. Apatite as an indicator mineral for mineral exploration: trace-element compositions and their relationship to host rock type. J. Geochem. Explor. 76, 45–69. https://doi.org/10.1016/S0375-6742(02)00204-2.
- Boiron, M.C., Cathelineau, M., Banks, D., Yardley, B., Noronha, F., Miller, F.M., 1996.
 P-T-X conditions of fluid penetration in the basement during retrograde metamorphism and uplift: a multidisciplinary investigation of bulk and individual fluid inclusion chemistry from NW Iberian quartz veins. Geochim. Cosmochim. Acta 60, 43–57.
- Blum, J.D., 1985. A pretologic and Rb-Sr isotopic study of intrusive rocks near Fairbanks. Alaska. Can. J. Earth Sci. 22, 1314–1321.
- Boiron, M.C., Cathelineau, M., Banks, D.A., Fourcade, S., Vallance, J., 2003. Mixing of metamorphic and surficial fluids during the uplift of the Hercynian upper crust: consequences for gold deposition. Chem. Geol. 194 (1–3), 119–141. https://doi.org/ 10.1016/S0009-2541(02)00274-7.
- Boutroy, E., Dare, S., Beaudoin, G., Barnes, S.-J., Lightfoot, P., 2014. Magnetite composition in Ni-Cu-PGE deposits worldwide and its application to mineral exploration. J. Geochem. Explor. 145, 64–81.
- Breiman, L., 2001. Random forests. Mach. Learn. 45 (5–32), 2001. https://doi.org/ 10.1023/A:1010933404324.
- Breiter, K., Ďurišová, J., Hrstka, T., Korbelová, Z., Vaňková, M.H., Galiová, M.V., Kanický, V., Rambousek, P., Knésl, I., Dobeš, P., Dosbaba, M., 2017a. Assessment of magmatic vs. metasomatic processes in rare-metal granites: a case study of the Cínovec/Zinnwald Sn-W-Li deposit, Central Europe. Lithos 292-293, 198-217. https://doi.org/10.1016/j.lithos.2017.08.015.
- Breiter, K., Korbelová, Z., Chládek, Š., Uher, P., Knesl, I., Rambousek, P., Honig, S., Šešulka, V., 2017b. Diversity of Ti–Sn–W–Nb–Ta oxide minerals in the classic granite-related magmatic-hydrothermal Cínovec/Zinnwald Sn–W–Li deposit (Czech Republic). Eur. J. Mineral. 29 (4), 727–738. https://doi.org/10.1127/ejm/2017/0029-2650.
- Bronac, De, de Vazelhes, V., 2019. Étude de la dispersion d'un gisement d'or dans les sédiments glaciaires: !Le cas d'Amaruq. Université Laval, Nunavut, Canada, p. 213p. M.Sc. thesis..
- De Bronac, de Vazelhes, V., Beaudoin, G., McMartin, I., Côté-Mantha, O., Boulianne-Verschelden, N., 2021. Assessment of the Amaruq gold deposit signature in glacial sediments using multivariate geochemical data analysis and indicator minerals.

 J. Geochem. Explor. 228, 106800.
- Brugger, J., Lahaye, Y., Costa, S., Lambert, D., Bateman, R., 2000. Inhomogeneous distribution of REE in scheelite and dynamics of Archaean hydrothermal systems (Mt Charlotte and Drysdale gold deposits, Western Australia). Contrib. Mineral. Petrol. 139, 251–264.
- Brugger, J., Etschmann, B., Pownceby, M., Liu, W., Grundler, P., Brewe, D., 2008. Oxidation state of europium in scheelite: tracking fluid–rock interaction in gold deposits. Chem. Geol. 257, 26–33.
- Burt, D., 1989. Compositional and phase relations among rare earth elements. Rev. Mineral. 21, 259–307.
- Candela, P.A., 1992. Controls on ore metal ratios in granite related ore systems: an experimental and computational approach: Royal Society of Edinburgh transactions. Earth Sci. 83, 317–326. https://doi.org/10.1017/S0263593300007999.

- Caraballo, E., Dare, S., Beaudoin, G., 2022. Variation of trace elements in chalcopyrite from worldwide Ni-Cu sulfide and Reef-type PGE deposits: implications for mineral exploration. Mineral. Deposita. 57, 1293–1321.
- Cave, B.J., 2016. Source of Scheelite in the Turbidite-Hosted Orogenic Au Deposits of Otago, New Zealand: An Integrated Metamorphic Source Model Explaining the Presence or Absence of Scheelite in Turbidite-Hosted Orongenic Au Deposits. PhD thesis, University of Tasmania.
- Cave, B.J., Pitcairn, İ.K., Craw, D., Large, R.R., Thompson, J.M., Johnson, S.C., 2017. A metamorphic mineral source for tungsten in the turbidite-hosted orogenic gold deposits of the Otago Schist, New Zealand. Mineral. Deposita 52, 515–537. https://doi.org/10.1007/s00126-016-0677-5.
- Cepedal, A., Fuertes-Fuente, M., Martin-Izard, A., Boixet, L., 2014. Tellurides, sulfides and sulfosalts in the mineral paragenesis of the Corcoesto orogenic gold deposit, NW Spain. In: Conference: IMA 2014 At: Sudafrica Volume. Abstract Volume ISBN: 978-0-620-60082-8. p 14.
- Cooke, D.R., Baker, M., Hollings, P., Sweet, G., Chang, Z., Danyushevsky, L., Gilbert, S., Zhou, T., White, N.C., Gemmell, J.B., Inglis, S., 2014. New Advances in Detecting the Distal Geochemical Footprints of Porphyry Systems—Epidote Mineral Chemistry as a Tool for Vectoring and Fertility Assessments, Building Exploration Capability for the 21st Century. Karen D. Kelley, Howard C. Golden.
- Cracknell, M.J., Reading, A.M., 2014. Geological mapping using remote sensing data: A comparison of five machine learning algorithms, their response to variations in the spatial distribution of training data and the use of explicit spatial information. Comput. Geosci. 63, 22–33.
- Craw, D., MacKenzie, D., Grieve, P., 2015. Supergene gold mobility in orogenic gold deposits, Otago Schist, New Zealand. N. Z. J. Geol. Geophys. 58, 123–136.
- Darbyshire, D.P.F., Pitfield, P.E.J., Campbell, S.D.G., 1996. Late Archean and Early Proterozoic gold-tungsten mineralization in the Zimbabwe Archean craton: Rb-Sr and Sm-Nd isotope constraints. Geology 24 (1), 19–22. https://doi.org/10.1130/ 0091-7613(1996)024<0019;LAAEPG>2.3.CO;2.
- Dare, S.A.S., Barnes, S.J., Beaudoin, G., 2012. Variation in trace element content of magnetite crystallized from a fractionating sulfide liquid, Sudbury, Canada: implications for provenance discrimination. Geochim. Cosmochim. Acta 88, 27–50. https://doi.org/10.1016/j.gca.2012.04.032.
- Dare, S.A.S., Barnes, S.J., Beaudoin, G., 2014. Trace elements in magnetite as petrogenetic indicators. Mineral. Deposita 49, 785–796. https://doi.org/10.1007/ s00126-014-0529-0.
- Dubru, M., Vander Auwera, J., Van Marcke De Lummen, G., Verkaeren, J., 1988.
 Distribution of scheelite in magnesian skarns at Traversella (Piemontese Alps, Italy) and Costabonne (Eastern Pyrenees, France): nature of the associated magmatism and influence of fluid composition. In: Boissonnas, J., Omenetto, P. (Eds.), Mineral Deposits within the European Community. Society for Geology Applied to Mineral Deposits, Special Publication 6, Springer-Verlag, Berlin, Germany, pp. 117–134.
- Dupuis, C., Beaudoin, G., 2011. Discriminant diagrams for iron oxide trace element fingerprinting of mineral deposit types. Mineral. Deposita 46, 319–335. https://doi. org/10.1007/s00126-011-0334-y.
- Duran, C., Dubé-Loubert, H., Page, P., Barnes, S.-J., Roy, M., Savard, D., Cave, B.J., Arguin, J.-P., Mansur, E., 2019. Applications of trace element chemistry of pyrite and chalcopyrite in glacial sediments to mineral exploration targeting: example from the Churchill Province, northern Quebec, Canada. J. Geochem. Explor. 196, 105–130.
- Einaudi, M.T., Hedenquist, J.W., Inan, E., 2003. Sulfidation state of fluids in active and extinct hydrothermal systems: T ransitions from porphyry to epithermal environments. Society of Economic Geologists Special Publication 10, 285–314.
- Elongo, V., Falck, H., Rasmussen, K.L., Robbins, L.J., Creaser, R.A., Luo, Y., Pearson, D. G., Sarkar, C., Adlakha, E., Palmer, M.C., Scott, J.M., Hickey, K., Konhauser, K., Lecumberri-Sanchez, P., 2022. Ancient roots of tungsten in western North America. Geology 50 (7), 791–795. https://doi.org/10.1130/G49801.1.
- Geology 50 (7), 791–795. https://doi.org/10.1130/G49801.1.
 Eriksson, L., Johansson, E., Kettaneh-Wold, N., Wold, S., 2001. Multi- and Megavariate
 Data Analysis, Principles and Applications. UMETRICS, Umea, p. 425.
- European Commission, 2017. Study on the Review of the List of Critical Raw Materials. Publication Office of the European Union, Critical Materials Factsheets. https://doi.org/10.2873/398823.
- Fuertes-Fuente, M., Cepedal, A., Lima, A., Dória, A., Ribeiro, M.A., Guedes, A., 2016. The Au-bearing vein system of the Limarinho deposit (northern Portugal): genetic constraints from Bi-chalcogenides and Bi-Pb-Ag sulfosalts, fluid inclusions and stable isotopes. Ore Geol. Rev. 72, 213–231. https://doi.org/10.1016/j. oregeorev.2015.07.009.
- Gaspar, M., Knaack, C., Meinert, L., Moretti, R., 2008. REE in skarn systems: a LA-ICP-MS study of garnets. Geochim. Cosmochim. Acta 72, 185–205. https://doi.org/10.1016/j.gca.2007.09.033.
- George, L., Cook, N., Ciobanu, C., Wade, B., 2015. Trace and minor elements in galena: a reconnaissance LA-ICP-MS study. Am. Mineral. 100, 548–569.
- George, L., Cook, N., Crowe, B., Ciobanu, C., 2018. Trace elements in hydrothermal chalcopyrite. Mineral. Mag. 82 (1), 59–88.
- Ghaderi, M., Palin, J., Campbell, I., Sylvester, P., 1999. Rare earth element systematics in scheelite from hydrothermal gold deposits in the Kalgoorlie-Norseman region, Western Australia. Econ. Geol. 94, 423–437.
- Ghosh, U., Upadhyay, D., 2022. The retrograde evolution of F-rich skarns: Clues from major and trace element chemistry of garnet, scheelite, and vesuvianite from the Belka Pahar wollastonite deposit, India. Lithos 422–423, 106750. https://doi.org/ 10.1016/j.lithos.2022.106750.
- Gillerman, V.S., Schmitz, M.D., Benowitz, J.A., Layer, P.W., 2019. Geology and temporal evolution of alteration and Au-Sb-W mineralization, Stibnite mining district, Idaho. Idaho Geological Survey Bulletin 31, 149 p.
- Goldfarb, R.G., Baker, T., Dubé, B., Groves, D.I., Hart, C.J.R., Gosselin, P., 2005. Distribution, character, and genesis of gold deposits in metamorphic Terran. In:

- Hedenquist, Jeffrey W., Thompson, John F.H., Goldfarb, Richard J., Richards, Jeremy P. (Eds.), One Hundredth Anniversary Volume.
- Gregory, D.D., Cracknell, M.J., Large, R.R., McGoldrick, P., Kuhn, S., Maslennikov, V.V., Baker, M.J., Fox, N., Belousov, I., Figueroa, M.C., Steadman, J.A., Fabris, A.J., Lyons, T.W., 2019. Distinguishing ore deposit type and barren sedimentary pyrite using laser ablation-inductively coupled plasma-mass spectrometry trace element data and statistical analysis of large data sets. Econ. Geol. 114 (4), 771–786.
- Groves, D.I., Goldfarb, R.J., Gebre-Mariam, M., Hagemann, S.G., Robert, F., 1998.
 Orogenic gold deposits: A proposed classification in the context of their crustal distribution and relationship to other gold deposit types. Or. Geol. 13, 7–27.
- Grzela, D., Beaudoin, G., Bedard, E., 2019. Tourmaline, scheelite, and magnetite compositions from orogenic gold deposits and glacial sediments of the Val-d'Or district (Quebec, Canada): implications to mineral exploration. J. Geochem. Explor. 206, 106355.
- Haas, J., Shock, E.L., Sassani, D., 1995. Rare earth elements in hydrothermal systems: estimates of standard partial molal thermodynamic properties of aqueous complexes of the rare earth elements at high. Geochim. Cosmochim. Acta 59, 4329–4350.
- Hart, C., 2007. Reduced intrusion-related gold systems. In: Goodfellow, In W.D. (Ed.), Mineral Deposits of Canada: A Synthesis of Major Depositypes, District Metallogeny, the Evolution of Geological Provinces, and Exploration Methods. Geological Association of Canada, Mineral Deposits Division, pp. 95–112.
- Hart, C.J.R., Baker, T., Burke, M.J., 2000. New exploration concepts for country-rock-hosted intrusion-related gold systems: Tintina Gold Belt in Yukon. In: The Tintina Gold Belt: Concepts, Exploration, and Discoveries, 2. British Columbia and Yukon Chamber of Mines Special Volume, pp. 145–171.
- Hart, C.J.R., McCoy, D.T., Goldfarb, R.J., Smith, M., Roberts, P., Hulstein, R., Bakke, A. A., Bundtzen, T.K., 2002. Geology, exploration and discovery in the Tintina Gold Province. In: Goldfarb, R.J., Neilson, R. (Eds.), Geology, Exploration and Discovery in the Tintina Gold Province, Alaska and Yukon, 9. Society of Economic Geologists Special, pp. 241–274.
- Hsu, L., 1977. Effects of oxygen and sulfur fugacities on the scheelite tungstenite and powellite-molybdenite stability relations. Econ. Geol. 72, 664–670.
- Hsu, L.C., Galli, P.E., 1973. Origin of the scheelite-powellite series of minerals. Econ. Geol. 68, 681–696.
- Huang, X.-W., Sappin, A.-A., Boutroy, E., Beaudoin, G., Makvandi, S., 2019. Trace element composition of igneous and hydrothermal magnetite from porphyry deposits: relationship to deposit subtypes and magmatic affinity. Econ. Geol. 114 (5), 917–952. https://doi.org/10.5382/econgeo.4648.
- Huang, X.-D., Lu, J.-J., Zhang, R.-Q., Sizaret, S., Ma, D.-S., Wang, R.-C., Zhu, X., He, Z.-Y., 2022. Garnet and scheelite chemistry of the Weijia tungsten deposit, South China: implications for fluid evolution and W skarn mineralization in F-rich ore system. Ore Geol. Rev. 142. 104729 https://doi.org/10.1016/j.orgegorev.2022.104729.
- Jochum, K.P., Nohl, U., Herwig, K., Lammel, E., Stoll, B., Hofmann, A.W., 2005. GeoReM: a new geochemical database for reference materials and isotopic standards. Geostand. Geoanal. Res. 29, 333–338.
- Kempe, U., Oberthur, Th., 1997. Physical and geochemical characteristics of scheelite from gold deposits: A reconnaissance study. Mineral Deposits, Papunen ed.
- Kempe, U., Belyatsky, B., Krymsky, R., Kremenetsky, A.A., Ivanov, P.A., 2001. Sm–Nd and Sr isotope systematics of scheelite from the giant Au(–W) deposit Muruntau (Uzbekistan): implications for the age and sources of Au mineralization. Mineral. Deposita 36, 379–392. https://doi.org/10.1007/s001260100156.
- Kent, A.J.R., Campbell, I.H., McCulloch, M.T., 1995. Sm-Nd systematics of hydrothermal scheelite from the Mount Charlotte Mine, Kalgoorlie, Western Australia; an isotopic link between gold mineralization and komatiites. Econ. Geol. 90 (8), 2329–2335. https://doi.org/10.2113/gsecongeo.90.8.2329.
- Keppler, H., 1993. Influence of fluorine on the enrichment of high field strength trace elements in granitic rocks. Contrib. Mineral. Petrol. 114, 479–488. https://doi.org/ 10.1007/BF00321752
- Kozlik, M., Gerdes, A., Raith, J.G., 2016a. Strontium isotope systematics of scheelite and apatite from the Felbertal tungsten deposit, Austria – results of in-situ LA-MC-ICP-MS analysis. Mineral. Petrol. 110, 11–27. https://doi.org/10.1007/s00710-015-0416-0.
- Kozlik, M., Raith, J.G., Gerdes, A., 2016b. U-Pb, Lu-Hf and trace element characteristics of zircon from the Felbertal scheelite deposit (Austria): new constraints on timing and source of W mineralization. Chem. Geol. 421, 112–126. https://doi.org/ 10.1016/j.chemgeo.2015.11.018.
- Kuhn, M., 2008. Building predictive models in R using the caret package. J. Stat. Softw. 28 (5), 1–26.
- Lang, J.R., Baker, T., 2001. Intrusion-related gold systems: the present level of understanding. Mineral. Deposita 36, 477–489. https://doi.org/10.1007/ s001260100184.
- Lecumberri-Sanchez, P., Vieira, R., Heinrich, C.A., Pinto, F., Wälle, M., 2017. 627. Fluid-rock interaction is decisive for the formation of tungsten deposits.628. Geology 45, 579–582.
- Legros, H., Lecumberri-Sanchez, P., Elongo, V., Laurent, O., Falck, H., Adlakha, E., Chelle-Michou, C., 2020. Fluid evolution of the Cantung tungsten skarn, Northwest Territories, Canada: Differentiation and fluid-rock interaction. Ore Geol. Rev, p. 127.
- Li, X.-Y., Gao, J.-F., Zhang, R.-Q., Lu, J.-J., Chen, W.-H., Wu, J.-W., 2018. Origin of the Muguayuan veinlet-disseminated tungsten deposit, South China: constraints from insitu trace element analyses of scheelite. Ore Geol. Rev. 99, 180–194. https://doi.org/ 10.1016/j.oregeorev.2018.06.005.
- Li, W., Xie, G.-Q., Mao, J.-W., Zhang, H.-C., 2021. Mineralogy, fluid inclusion and isotope signatures: implications for the genesis of the Early Paleozoic Yangjiashan scheelitequartz vein deposit, South China. Ore Geol. Rev. 134, 104136 https://doi.org/ 10.1016/j.oregeorev.2021.104136.

- Liu, H., Beaudoin, G., 2021. Geochemical signatures in native gold derived from Aubearing ore deposits. Ore Geol. Rev. 132, 104066 https://doi.org/10.1016/j.oregeorev.2021.104066.
- Liu, Z., Hollings, P., Mao, X., Lawley, C.J.M., Yang, B., Tang, L., 2021. Metal remobilization from country rocks into the Jiaodong-type orogenic gold systems, Eastern China: new constraints from scheelite and galena isotope results at the Xiadian and Majiayao gold deposits. Ore Geol. Rev. 134, 104126.
- Liu, B., Li, H., Liu, Y.-G., Algeo, T.J., Luo, X.-T., Girei, M.B., Wu, Q.-H., Hua Kong, H., Zhang, D.X., Jiang, J.-B., 2022. Crystallization processes and genesis of scheelite in a quartz vein-type W deposit (Xianghuapu, South China). Chem. Geol. 613, 121142.
- Mair, J.L., Goldfarb, R.J., Johnson, C.A., Hart, C.J.R., Marsh, E.E., 2006. Geochemical constraints on the genesis of the Scheelite dome intrusion-related gold deposit, Tombstone gold belt, Yukon, Canada. Econ. Geol. 101, 523–553.
- Makvandi, S., Beaudoin, G., McClenaghan, B., Quirt, D., Ledru, P., 2019. PCA of Feoxides MLA data as an advanced tool in provenance discrimination and indicator mineral exploration: case study from bedrock and till from the Kiggavik U deposits area (Nunavut, Canada). J. Geochem. Explor. 197, 199–211. https://doi.org/10.1016/j.gexplo.2018.11.013.
- Maloof, T.L., Baker, T., Thompson, J.F., 2001. The Dublin Gulch intrusion-hosted gold deposit, Tomb-stone plutonic suite, Yukon Territory, Canada. Mineral. Deposita 36, 583–593. https://doi.org/10.1007/s001260100190.
- Maneglia, N., Beaudoin, G., Simard, M., 2017. Indicator minerals of the Meliadine orogenic gold deposits, Nunavut (Canada), and application to till surveys. Geochem Explor Environ Anal 18, 241–251.
- Mansur, E.T., Barnes, S.J., Duran, C.J., Sluzhenikin, S.F., 2020. Distribution of chalcophile and platinum-group elements among pyrrhotite, pentlandite, chalcopyrite and cubanite from the Noril'sk-Talnakh ores: Implications for the formation of platinum-group minerals. Mineral. Deposita 55 (6), 1215–1232.
- Mansur, E.T., Barnes, S.-J., Duran, C., 2021. An overview of chalcophile element contents of pyrrhotite, pentlandite, chalcopyrite, and pyrite from magmatic Ni-Cu-PGE sulfide deposits. Mineral. Deposita 56, 179–204.
- Mansur, E.T., Dare, S.A.S., Ferreira Filho, C.F., Miranda, A.C.R., Monteiro, L.V.S., 2023. The distribution of trace elements in sulfides and magnetite from the Jaguar hydrothermal nickel deposit: exploring the link with IOA and IOCG deposits within the Carajás Mineral Province, Brazil. Ore Geol. Rev. 152, 105256 https://doi.org/ 10.1016/j.oregeorev.2022.105256.
- Mao, M., Rukhlov, A., Rowins, S., Spence, J., Coogan, L., 2016. Apatite trace element compositions: a robust new tool for mineral exploration. Econ. Geol. 111, 1187–1222.
- McClenaghan, M., Parkhill, M., Pronk, A., Seaman, A., McCurdy, M., Leybourne, M., 2017. Indicator mineral and geochemical signatures associated with the Sisson W-Mo deposit, New Brunswick, Canada. Geochem Explor Environ Anal 17, 297–313.
- McDonough, W.F., Sun, S.S., 1995. The composition of the earth. Chem. Geol. 120, 223–253.
- Migdisov, A., Williams-Jones, A.E., Brugger, J., Caporuscio, F., 2016. Hydrothermal transport, deposition, and fractionation of REE: experimental data and thermodynamic calculations. Chem. Geol. 439, 13-42.
- Mihalynuk, M.G., Heaman, L.M., 2002. Age of mineralizated porphyry at the Logtung deposit W-Mo-Bi-Be (beryl, aqua- marine), northwest BC. Geological Fieldwork, BC Ministry of Energy and Mines 35–39.
- Miller, C.F., Mittlefehldt, D.W., 1984. Extreme fractionation in felsic magma chambers: a product of liquid-state diffusion or fractional crystallization? Earth Planet. Sci. Lett. 68, 151, 158, https://doi.org/10.1016/0012
- 68, 151–158. https://doi.org/10.1016/0012-821X(84)90147-X. Miller, C.F., Stoddard, E.F., 1981. The role of manganese in the paragenesis of magmatic garnet: an example from the Old Woman-Piute Range, California. J. Geol. 89, 770–772
- Miranda, A.C.R., Beaudoin, G., Rottier, B., 2022. Scheelite chemistry from skarn systems: implications for ore-forming processes and mineral exploration. Mineral. Deposita. https://doi.org/10.1007/s00126-022-01118-y.
- Mutch, A.R., 1969. The scheelite resources of the Glenorchy district, west Otago. New Zealand Geological Survey report 40.
- Myint, A.Z., Yonezu, K., Boyce, A.J., Selby, D., Scherstén, A., Tindell, T., Watanabe, K., Swe, Y.M., 2018. Stable isotope and geochronological study of the Mawchi Sn-W deposit, Myanmar: implications for timing of mineralization and ore genesis. Ore Geol. Rev. 95, 663–679. https://doi.org/10.1016/j.oregeorev.2018.03.014.
- Nassau, K., 1963. Calcium tungstate—IV: the theory of coupled substitution. J. Phys. Chem. Solids 24, 1511–2151.
- Nathwani, C.L., Wilkinson, J.J., Fry, G., Armstrong, R.N., Smith, D.J., Ihlenfeld, C., 2022. Machine learning for geochemical exploration: classifying metallogenic fertility in arc magmas and insights into porphyry copper deposit formation. Mineral. Deposita 57, 1143–1166. https://doi.org/10.1007/s00126-021-01086-9.
- Neiva, A.M.R., Moura, A., Leal Gomes, C.A., Pereira, M.F., Corfu, F., 2019. The granite-hosted Variscan gold deposit from Santo António mine in the Iberian Massif (Penedono, NW Portugal): constraints from mineral chemistry, fluid inclusions, sulfur and noble gases isotopes. J. Iber. Geol. 45, 443–469. https://doi.org/10.1007/s41513-019-00103-1.
- Newberry, R., Swanson, S., 1986. Scheelite skarn granitoids: an evaluation of the roles of magmatic source and process. Ore Geol. Rev. 1, 57–81.
- Nguyen, T.H., Nevolko, P.A., Pham, T.D., Svetlitskaya, T.V., Tran, T.H., Shelepaev, R.A., Fominykh, P.A., Pham, N.C., 2020. Age and genesis of the W-Bi-Cu-F (Au) Nui Phao deposit, Northeast Vietnam: constrains from U-Pb and Ar-Ar geochronology, fluid inclusions study, S-O isotope systematic and scheelite geochemistry. Ore Geol. Rev. 123, 103578 https://doi.org/10.1016/j.oregeorev.2020.103578.
- Nie, L., Wang, F., White, N.C., Zhang, D., Yan, C., Wang, X., 2023. Scheelite trace element compositions: a robust new tool for mineral exploration. Ore Geol. Rev. 155, 105338.

- Noble, S.R., Spooner, E.T.C., Harris, F.R., 1984. The Logtung large tonnage, low-grade W (scheelite)-Mo porphyry deposit, south-central Yukon Territory. Econ. Geol. 79 (5), 848–868. https://doi.org/10.2113/gsecongeo.79.5.848.
- O'Brien, J., Spry, P., Teale, G., Jackson, S., Koenig, A., 2015. Gahnite composition as a means to fingerprint metamorphosed massive sulfide and non-sulfide zinc deposits. J. Geochem. Explor. 159, 48–61.
- Palarea-Albaladejo, J., Martin-Fernandez, J.A., 2013. Values below detection limit in compositional chemical data. Anal. Chim. Acta 764, 32–43.
- Palarea-Albaladejo, J., Martin-Fernandez, J.A., 2015. zCompositions-R package for multivariate imputation of left-censored data under a compositional approach. Chemom. Intell. Lab. Syst. 143, 85–96.
- Palmer, M.C., 2021. Geochemical Characterisation of Scheelite from New Zealand (Thesis, Doctor of Philosophy). University of Otago. Retrieved from. http://hdl.han dle.net/10523/12254.
- Palmer, M.C., Scanlan, E.J., Scott, J.M., Farmer, L., Pickering, D., Wilson, V.J., Oelze, M., Craw, D., le Roux, P.J., Luo, Y., Graham, D.G., Reid, M.R., Stirling, C.H., 2022. Distinct scheelite REE geochemistry and 87Sr/86Sr isotopes in proximally- and distally-sourced metamorphogenic hydrothermal systems, Otago Schist, New Zealand. Ore Geol. Rev. 144, 104800 https://doi.org/10.1016/j.oregeorev.2022.104800.
- Pan, J.Y., Ni, P., Wang, R.C., 2019. Comparison of fluid processes in coexisting wolframite and quartz from a giant vein-type tungsten deposit, South China: insights from detailed petrography and LA-ICP-MS analysis of fluid inclusions. Am. Mineral. 104, 1092–1116.
- Pašava, J., Svojtka, M., Veselovský, F., Ďurišová, J., Ackerman, L., Pour, O., Drábek, M., Halodová, P., Haluzová, E., 2016. Laser ablation ICPMS study of trace element chemistry in molybdenite coupled with scanning electron microscopy (SEM) an important tool for identification of different types of minerali- zation. Ore Geol. Rev. 72, 874–895. https://doi.org/10.1016/j.oregeorev.2015.09.007.
- Paterson, C.J., Rankin, P.C., 1979. Trace element distribution in the schist surrounding a quartz-scheelite lode, Glenorchy, New Zealand. N. Z. J. Geol. Geophys. 22 (3), 329–338. https://doi.org/10.1080/00288306.1979.10424102.
- Paton, C., Hellstrom, J., Paul, B., Woodhead, J., Hergt, J., 2011. Iolite: freeware for the visualization and processing of mass spectrometric data. J. Anal. At. Spectrom. 26, 2508–2518. https://doi.org/10.1039/c1ja10172b.
- Piccoli, P.M., Candela, P.A., 2002. Apatite in Igneous Systems. Rev. Mineral. Geochem. 48 (1), 255–292. https://doi.org/10.2138/rmg.2002.48.6.
- Pirajno, F., Bentley, P.N., 1985. Greisen-related scheelite, gold and sulphide mineralisation at Kirwans Hili and Bateman Creek, Reefton district, Westland, New Zealand. N. Z. J. Geol. Geophys. 28, 97–109.
- Pollard, P.J., Pichavant, M., Charoy, B., 1987. Contrasting evolution of fluorine- and boron-rich tin systems. Mineral. Deposita 22, 315–321. https://doi.org/10.1007/ BE00204525
- Porter, J., McNaughtona, N., Evansa, N., McDonald, J., 2020. Rutile as a pathfinder for metals exploration. Ore Geol. Rev. 120, 03406.
- Poulin, R., Kontak, D., McDonald, A., McClenaghan, M., 2018. Assessing scheelite as an ore-deposit discriminator using its trace element and REE chemistry. Can. Mineral. 56, 265–302.
- R Core Team, 2021. R: A Language and Environment for Statistical Computing. R
 Foundation for Statistical Computing, Vienna, Austria. URL. https://www.R-project.
- Raith, J.G., Gerdes, A., Cornell, D.H., 2011. In situ U–Pb dating of scheelite: constraints on the age and genesis of the Felbertal tungsten deposit. Mineral. Mag. 75, 1690. Rodriguez-Galiano, V., Sanchez-Castilho, M., Chica-Olmo, M., Chica-Ricas, M., 2015.
- Rodriguez-Gallano, V., Sanchez-Castlino, M., Chica-Olmo, M., Chica-Ricas, M., 2015. Machine learning predictive models for mineral prospectivity: An evaluation of neural networks, random forest, regression trees and support vector machines. Ore Geol. Rev. 71, 804–818.
- Rohart, F., Gautier, B., Singh, A., Le Cao, K.-A., 2017. mixOmics: an R package for 'omics feature selection and multiple data integration. PLoS Comput. Biol. 13 (11), e1005752
- Roper, M.W., 2008. Jennings project report on 2008 Diamond Drill hole J08-08 Yukon quartz claim hot 19 Yukon Territory. Agnico-Eagle Mines Limited.
- Rottier, B., Casanova, V., 2020. Trace element composition of quartz from porphyry systems: a tracer of the mineralizing fluid evolution. Mineral. Deposita 55, 843–862.
- Scanlan, E.J., Scott, J.M., Wilson, V.J., Stirling, G.H., Reid, M.R., Le Roux, P.J., 2018. In Situ ⁸⁷Sr/⁸⁶Sr of scheelite and calcite reveals proximal and distal fluid-rock interaction during orogenic W-Au mineralization, otago schist, New Zealand. Econ. Geol. 113 (7), 1571–1586. https://doi.org/10.5382/econgeo.2018.4603.
- Sciuba, M., Beaudoin, G., Grzela, D., Makvandi, S., 2020. Trace element composition of scheelite in orogenic gold deposits. Mineral. Deposita 55, 1149–1172.
- Sciuba, M., Beaudoin, G., Makvandi, S., 2021. Chemical composition of tourmaline in orogenic gold deposits. Mineral. Deposita 56, 537–560.
- Seo, J.H., Yoo, B.C., Yang, Y.S., Lee, J.H., Jang, J., Shin, D., 2020. Scheelite geochemistry of the Sangdong W-Mo deposit and W prospects in the southern Taebaeksan metallogenic region, Korea. Geosci. J. 24, 701–721. https://doi.org/10.1007/ s12303-020-0005-z.
- Sha, L.-K., Chappell, Bruce W., 1999. Apatite chemical composition, determined by electron microprobe and laser-ablation inductively coupled plasma mass spectrometry, as a probe into granite petrogenesis. Geochim. Cosmochim. Acta 63, 3861–3881. https://doi.org/10.1016/S0016-7037(99)00210-0.
- Sims, J., 2018. Fort Knox Mine Fairbanks North Star Borough. Kinross Gold Corporation, Alaska, USA. National Instrument 43-101 Technical Report.
- Song, G., Qin, K., Li, G., Evans, N., Chen, L., 2014. Scheelite elemental and isotopic signatures: Implications for the genesis of skarn-type W-Mo deposits in the Chizhou area, Anhui Province Eastern China. Am. Mineral. 99, 303–317.

- Stekhoven, D.J., Bühlmann, P., 2012. MissForest—non-parametric missing value imputation for mixed-type data. Bioinformatics 28, 112–118. https://doi.org/ 10.1093/bioinformatics/btr597.
- Štemprok, M., Mašková, A., 1992. Scheelite mineralization of the Bohemian Massif. Zbl. Geol. Palaont. Teil 1/2, 117–129.
- Sun, K., Chen, B., 2017. Trace elements and Sr-Nd isotopes of scheelite: implications for the W-Cu-Mo polymetallic mineralization of the Shimensi Deposit, south China. Am. Mineral. 102, 1114–1128.
- Sun, K., Chen, B., Deng, J., 2019. Ore genesis of the Zhuxi supergiant W-Cu skarn polymetallic deposit, South China: evidence from scheelite geochemistry. Ore Geol. Rev. 107, 14–29.
- Sun, G., Zeng, Q., Zhou, J.-X., 2022. Machine learning coupled with mineral geochemistry reveals the origin of ore deposits. Ore Geol. Rev. 142, 104753.
- Sverjensky, D., 1984. Europium redox equilibria in aqueous solution. Earth Planet. Sci. Lett. 67, 70–78.
- Thompson, J., Sillitoe, R., Baker, T., Lang, J.R., Mortensen, J.K., 1999. Intrusion-related gold deposits associated with tungsten-tin provinces. Mineral. Deposita 34, 323–334. https://doi.org/10.1007/s001260050207.
- Tyson, R.M., Hemphill, W.R., Theisen, A.R., 1988. Effect of the W:Mo ratio on the shift of excitation and emission spectra in the scheelite-powellite series. Am. Mineral. 73 (9–10), 1145–1154.
- Vallance, J., Cathelineau, M., Boiron, M.C., Fourcade, S., Shepherd, T.J., Naden, J., 2003. Fluid-rock interactions and the role of late Hercynian aplite intrusion in the genesis of the Castromil gold deposit, northern Portugal. Chem. Geol. 194, 201–224. https:// doi.org/10.1016/S0009-2541(02)00278-4.
- Veselovský, F., Ackerman, L., Pašava, J., Žák, K., Haluzová, E., Creaser, R.A., Dobeš, P., Erban, V., Tasler, R., 2018. Multiphase formation of the Obří důl polymetallic skarn deposit, West Sudetes, Bohemian Massif: geochemistry and Re–Os dating of sulfide mineralization. Mineral. Deposita 53, 665–682. https://doi.org/10.1007/s00126-017-0766-0.
- Voicu, G.M., Bardoux, M., Stevenson, R., Jebrak, M., 2001. Nd and Sr isotope study of hydrothermal scheelite and host rocks at Omai, Guiana Shield: implications for ore fluid source and flow path during the formation of orogenic gold deposits. Mineral. Deposita 35, 302–314.
- Wade, C.E., Payne, J.L., Barovich, K., Gilbert, S., Wade, B.P., Crowley, J.L., Reid, A., Jagodzinski, E.A., 2022. Zircon trace element geochemistry as an indicator of magma fertility in iron oxide copper-gold provinces. Econ. Geol. 117 (3), 703–718. https://doi.org/10.5382/econgep.4886.
- Wang, X.-S., Williams-Jones, A.E., Hu, R.-Z., Shang, L.-B., Bi, X.-W., 2021. The role of fluorine in granite-related hydrothermal tungsten ore genesis: results of experiments

- and modeling. Geochim. Cosmochim. Acta 292, 170–187. https://doi.org/10.1016/i.gca.2020.09.032.
- Webster, J., Thomas, R., Förster, H.J., Seltmann, R., Tappen, C., 2004. Geochemical evolution of halogen-enriched granite magmas and mineralizing fluids of the Zinnwald tin-tungsten mining district, Erzgebirge, Germany. Mineral. Deposita 39, 452–472. https://doi.org/10.1007/s00126-004-0423-2.
- Wilkinson, J.J., Chang, Z., Cooke, D.R., Baker, M.J., Wilkinson, C.C., Inglis, S., Chen, H., Gemmell, J.B., 2015. The chlorite proximitor: a new tool for detecting porphyry ore deposits. J. Geochem. Explor. 152, 10–26.
- Wintzer, N.E., Schmitz, M.D., Gillerman, V.S., Vervoort, J.D., 2022. U-Pb scheelite ages of tungsten and antimony mineralization in the Stibnite-Yellow Pine District, Central Idaho. Econ. Geol. https://doi.org/10.5382/econgeo.4953.
- Wood, S.A., Samson, I.M., 2000. The Hydrothermal Geochemistry of Tungsten in Granitoid Environments: I. Relative Solubilities of Ferberite and Scheelite as a Function of T, P, pH, and mNaCl. Econ. Geol. 95, 143–182.
- Wu, S., Mao, J., Ireland, T., Zaho, Z., Yao, F., Yang, Y., Sun, W., 2019. Comparative geochemical study of scheelite from the Shizhuyuan and Xianglushan tungsten skarn deposits, South China: implications for scheelite mineralization. Ore Geol. Rev. 109, 448, 464.
- Xu, J., Ciobanu, C., Cook, N.C., Slattery, A., 2019. Crystals from the powellite-scheelite series at the nanoscale: a case study from the Zhibula Cu skarn, Gangdese Belt. Tibet Minerals 9, 340.
- Yuan, L., Chi, G., Wang, M., Li, Z., Xu, D., Deng, T., Geng, J., Hu, M., Zhang, L., 2019. Characteristics of REEs and trace elements in scheelite from the Zhuxi W deposit, South China: implications for the ore forming conditions and processes. Ore Geol. Rev. 109, 585–597.
- Žáček, V., 2008. Cu-skarn v Kotli v Krkonoších (Česká republika). Bull. mineral.-petrolog. Odd. Nár. Muz. (Praha) 16 (2), 230–237. ISSN: 1211-0329
- Zhang, Q., Zhao, K.D., Li, W.-Q., Palmer, M.R., Jiang, S.-Y., Jaing, H., Zhang, W., Zhang, D., Hussian, A., 2022. Timing and tectonic setting of tin mineralization in southern Myanmar: constraints from cassiterite and wolframite U–Pb ages. Mineral. Deposita 57, 977–999. https://doi.org/10.1007/s00126-021-01083-y.
- Zhao, W., Zhou, M.-F., Williams-Jones, A., Zhao, Z., 2018. Constraints on the uptake of REE by scheelite in the Baoshan tungsten skarn deposit, South China. Chem. Geol. 477, 123–136.
- Zhao, L., Zhang, Y., Shao, Y., Li, H., Shah, S.A., Zhou, W., 2021. Using garnet geochemistry discriminating different skarn mineralization systems: perspective from Huangshaping W-Mo-Sn-Cu polymetallic deposit, South China. Ore Geol. Rev. 138